Acta Mechanica

A coupled meshfree-mesh based solution scheme on hybrid grid for flow induced vibrations

--Manuscript Draft--

Manuscript Number:	ACME-D-15-00558R1
Full Title:	A coupled meshfree-mesh based solution scheme on hybrid grid for flow induced vibrations
Article Type:	Original Paper
Keywords:	Fluid Structure Interaction; Meshfree Methods; Hybrid grid; RBF-FD; Partitioned FSI; Aeroelasticity
Corresponding Author:	Ali Javed, PhD Southampton, Hampshire UNITED KINGDOM
Corresponding Author Secondary Information:	
Corresponding Author's Institution:	
Corresponding Author's Secondary Institution:	
First Author:	Ali Javed, PhD
First Author Secondary Information:	
Order of Authors:	Ali Javed, PhD
	Kamal Djijdeli, PhD
	Jing T. Xing, PhD
Order of Authors Secondary Information:	
Funding Information:	
Abstract:	In this paper, a coupled meshfree-mesh based fluid solver is employed for flow induced vibration problems. Fluid domain comprises of a hybrid grid which is formed by generating a body conformal meshfree nodal cloud around the solid object and a static Cartesian grid which surrounds the meshfree cloud in the far field. The meshfree nodal cloud provides flexibility in dealing with solid motion by moving and morphing along with the solid boundary without necessitating re-meshing, and the Cartesian grid, on the other hand, provides improved performance by allowing the use of computationally efficient mesh based method. Flow equations, in Arbitrary Lagrangian-Eulerian (ALE) formulation, are solved by local Radial Basis Function in Finite Difference mode (RBF-FD) on moving meshfree nodes. Conventional finite differencing is used over static Cartesian grid for flow equations in Eulerian formulation. The equations for solid motion are solved using classical Runge Kutta method. Closed coupling is introduced between fluid and structural solvers by using a sub-iterative prediction-correction algorithm. In order to reduce computational overhead due to sub-iterations, only near field flow (in meshfree zone) is solved during inner iterations, and the full fluid domain is solved during outer (time step) iterations only when the convergence at solid-fluid interface has already been reached. In meshfree zone, adaptive sizing of influence domain has been introduced to maintain suitable number of neighbouring particles. The use of hybrid grid has been found to be useful in improving the computational performance by faster computing over Cartesian grid as well as by reducing the number of computations in the fluid domain during fluid-solid coupling. The solution scheme was tested for problems relating to flow induced cylindrical and airfoil vibration with one and two degrees of freedom. The results are found to be in good agreement with previous work and experimental results.

Engineering and the Environment

UNIVERSITY OF Southampton

The Editor and Reviewers,

Acta Mechanica

18 January 2016

Dear Sir/Madam,

Revised Manuscript: A coupled meshfree-mesh based solution scheme on hybrid grid for flow induced vibrations

Manuscript Reference No: ACME-D-15-00558

Reference: Your email on 04 January, 2016

We gratefully acknowledge the feedback about the manuscript. The comments from anonymous reviewers are found to be quite useful. Necessary amendments have been incorporated in the manuscript to account for the remarks by the reviewers. The comments from the reviewers are reproduced below, accompanied with point-by-point responses illustrating how the manuscript has been changed based on the reviews comments rovided therein.

It is believed that the attached submission fulfils the journal requirements you will consider it ready for publication in Acta Mechanica.

Sincerely,

Sincerely,

(Ali Javed)
Corresponding Author

Comments	Reply
Remarks of Reviewer-1	
Comment-1 I do not understand how the pressure problem is solved across the different domains. Being the pressure problem an elliptic problem, it should be solved directly in the whole domain considered otherwise some errors are introduced. It seems that in the outer region, where the Cartesian mesh is used, a Dirichlet velocity condition is prescribed on the inner boundary (Cat-III points). Which conditions are imposed for the pressure on these points? How is solved the pressure problem in the mesh-less domain? Where are imposed the Boundary Conditions for the pressure in the mesh-less domain? Can the authors provide a detailed description of these important aspects?	The pressure problem is set up separately in each domain (meshfree and Cartesian zones). In each time step, de-coupled momentum equations and pressure poison equation (Eqs. (5) to (7)) are first solved in meshfree zone. The governing equations are then solved in Cartesian zone. During solution of Eqs. (5) to (7) on Cartesian zone, the values of pressure and velocity at Cat-III nodes are used as boundary conditions on inner boundary (interface of the two zones) of Cartesian zone. In order to further clarify this, the words 'field parameters' are replaced by the words 'field parameters (pressure and velocity values)' in line 272, 298 and 308 respectively. Nevertheless, the idea coined by the reviewer is quite interesting. Instead of solving separate pressure problems in meshfree and Cartesian zones, a single problems can be setup, for pressure, in the entire domain. The proposed scheme is similar to what was used by Peng and Street in 1991 (A coupled multigrid domain-splitting technique for simulating incompressible flows in geometrically complex domains). It is likely that this will improve the accuracy of the solution. However, simultaneous solution for pressure will compromise the modular characteristics of the solution scheme. Currently, the meshfree and mesh based solvers run independent to each other exchanging data at the interface nodes. Simultaneous solution of pressure equations over the entre domain would require the derivation of a separate pressure equation applicable to all the zones. Further research can however be conducted in this direction. For this purpose, remarks have been included in the conclusion section of the manuscript (line 819 - 831).

Comment-2 In the final part of the Introduction there is a detailed description of the proposed method (more than 1 page). I think that it could be reduced since it is a repetition of what shown in the successive sections. On the other hand, I think that other methods recently adopted in simulating moving objects need to be discussed in the introduction. E.g. The Immersed Boundary Method, see e.g. Uhlmann JCP 2005, Picano et al. JFM2015.	As suggested by the reviewer, the description of current method in the introduction section is reduced. Moreover, a description of various grid generation techniques has been (including immersed boundary methods suggested by the reviewer) is included in the introduction (line 33 - 47).
Comment-3 In order to be easier to read, several figures need to be regenerated making larger plots and labels. E.g. fig 13, 14 (color codes are missing), 15, 19, 24	All the figures have been enlarged to improve readability.
Comment-4 There are some typos. E.g. pg 5. l.98 Arbitrary, pg.10 ln 202 Multiquadratic	The typos have been corrected. Moreover, a review of the manuscript has been made to ensure that it is free from such mistakes.
Remarks of Reviewer-2	
Comment-1 The only minor points concern the quality of figures 5-8 where it's hard to discern graphically the different categories of points.	The figures have been enlarged in order to improve their readability.

Noname manuscript No.
(will be inserted by the editor)

A. Javed · K. Djijdeli · J. T. Xing

A coupled meshfree-mesh based solution scheme on hybrid grid for flow induced vibrations

Received: date / Accepted: date

Abstract In this paper, a coupled meshfree-mesh based fluid solver is employed for flow induced vibration problems. Fluid domain comprises of a hybrid grid which is formed by generating a body conformal meshfree nodal cloud around the solid object and a static Cartesian grid which surrounds the meshfree cloud in the far field. The meshfree nodal cloud provides flexibility in dealing with solid motion by moving and morphing along with the solid boundary without necessitating re-meshing. The Cartesian grid, on the other hand, provides improved performance by allowing the use of computationally efficient mesh based method. Flow equations, in Arbitrary Lagrangian-Eulerian (ALE) formulation, are solved by local Radial Basis Function in Finite Difference mode (RBF-FD) on moving meshfree nodes. Conventional finite differencing is used over static Cartesian grid for flow equations in Eulerian formulation. The equations for solid motion are solved using classical Runge Kutta method. Closed coupling is introduced between fluid and structural solvers by using a sub-iterative prediction-correction algorithm. In order to reduce computational overhead due to sub-iterations, only near field flow (in meshfree zone) is solved during inner iterations. The full fluid domain is solved during outer (time step) iterations only when the convergence at solid-fluid interface has already been reached. In meshfree zone, adaptive sizing of influence domain is introduced to maintain suitable number of neighbouring particles. The use of hybrid grid has been found to be useful in improving the computational performance by faster computing over Cartesian grid as well as by reducing the number of computations in the fluid domain during fluid-solid coupling. The solution scheme was tested for problems relating to flow induced cylindrical and airfoil vibration with one and two degrees of freedom. The results are found to be in good agreement with previous work and experimental results.

Keywords Fluid Structure Interaction · Meshfree Methods · Hybrid grid · RBF-FD · Partitioned FSI · Aeroelasticity

1 Introduction

Meshfree methods refer to the class of computational techniques in which, at least, the structure of mesh is eliminated and the solution is approximated over a set of arbitrarily distributed data points (or nodes). In the absence of pre-specified grid connectivity constraint, computational nodes can be moved, added or removed more flexibly, from computational domain, during the simulation. Owing to these features, meshfree methods are considered to be better suited for problems involving large deformation, moving boundaries and complex geometries [6]. However, meshfree methods developed so far, are in general, computationally more expensive than conventional mesh based methods.

Radial Basis Functions (RBF) are primarily used for multivariate data interpolation over scattered data points. They are 'truly' meshfree in nature and can be also be used for solution of differential

A. Javed · K. Djijdeli · J. T. Xing
Faculty of Engineering and Environment, University of Southampton, UK
E-mail: salijav@hotmail.com

equations. In this regard, pioneering work was carried out by Kansa [33] who proposed the use of multiquadric RBFs for solution of flow equations over randomly distributed data points. Since then, use of RBFs for various flow problems has widely been investigated [4,58,38,59,40,25]. Initially, global RBFs were used for flow problems which used global domain for interpolation at a particular data point (or node). They are spectrally accurate. However, one of the difficulties faced while using global RBFs is that the problem tends to become ill-conditioned by increasing the number of data points within the interpolation region. As a result, maximum number of nodes and their distribution within the domain is limited by ill-conditioning effect. The limitation was later overcome by the use of local RBFs which compromise on spectral accuracy in bargain of better conditioned problems with improved accuracy [3,55,48,41]. This is done by localizing the influence domain around each particle. As a result, sparse and well conditioned coefficient matrices are generated irrespective of total number of data points and their density within the domain. RBF in Finite Difference mode [55,48,41,60] and RBF based differential quadrature methods [3] are the two famous local RBF techniques which are used for the solution of Navier Stokes equations in meshfree domain. However, like other meshfree methods, RBF based methods also suffer from high computational cost.

Grid generation methods for flow around moving bodies can be classified into boundary fitted and non-boundary fitted methods. The computational nodes of boundary fitted fluid grid exactly coincide with the fluid-solid interface [5,54,6,22]. The boundary conditions can therefore, directly be applied to the grid points and motion of the solid is explicitly tracked by the movement of grid points. On the contrary, non-boundary fitted methods employ a background mesh with solid boundary embedded on it. The background mesh can either be standard Cartesian, as used by [9] and [13] for inviscid flows, or unstructured grid, such as those used by [26,57] and [44] in the so-called immersed boundary methods. Non-boundary fitted methods greatly simplify the grid generation process and do not suffer from grid distortion around complex shapes. Moreover, re-meshing is not required to accommodate moving boundaries. However, the solid boundary may cut the background mesh in an arbitrary manner which may adversely affect the accuracy. Moreover, the precise control of grid resolution in the boundary layer region may not be possible.

Composite grids and domain decomposition techniques are often used for boundary fitted mesh-based methods to overcome the difficulty posed by complex geometries [43,27,8]. Hinatsu [27] proposed a multigrid method for geometrically complex flow problems. Perng and Street [43] used a domain decomposition technique for flow in regions with complex geometries. They solved flow momentum equation in each sub domain separately. However, pressure field was computed simultaneously in the entire domain. Recently multigrid methods have been proposed for hybrid meshfree and mesh-based grids, by [6,17] and [30], to minimize the computational overheads caused by the use of meshfree methods. These techniques introduce composite meshes comprising of meshfree and meshed zones in different parts of fluid domains. The aim is to optimize the performance by limiting the use of computationally expensive meshfree method only to the regions where it can actually outclasses mesh-based method in dealing with moving boundaries or complex geometries. Ding et al. [17] proposed a hybrid grid consisting of body conformal meshfree cloud embedded over a background Cartesian grid for static problems. In that, a coupled solution scheme, employing moving least square finite difference (MLSFD) on meshfree cloud and central differencing on Cartesian grid, was used. Chew et al. [6] extended similar approach to the moving objects. They used generalized finite difference (GFD) approximation in weighted least square (WLS) form over meshfree zone.

Flow induced solid vibration is a subject of fluid structure interaction (FSI). Such problems can be modelled either with monolithic or partitioned approach. In monolithic schemes, fluid and structural equations are reformulated, combined and then solved simultaneously using single time integration method [32]. The method sounds appealing as it provides single set of equations for mathematical analysis and does not pose inaccuracies at fluid-structure interface [20]. However, difference in mathematical properties of fluid and solid subsystems, issues related to software modularities and loss of generalization for usability of solution scheme strictly limit their widespread application [20]. On the contrary, partitioned procedures, employing separate time integration schemes for fluid and structure subsystems, are used more often for FSI problems and particularly for non-linear aero-elasticity [42,20,19,12,18,29,45,32]. Partitioned procedures provide flexibility of choosing different solvers for fluid and structure subsystems. However, the coupling errors, at fluid-solid interface, are often advocated as limitation to this approach. Such inveteracies are more pronounced in loosely coupled systems where solutions from fluid and structural subsystems are not necessarily converged at the interface boundary

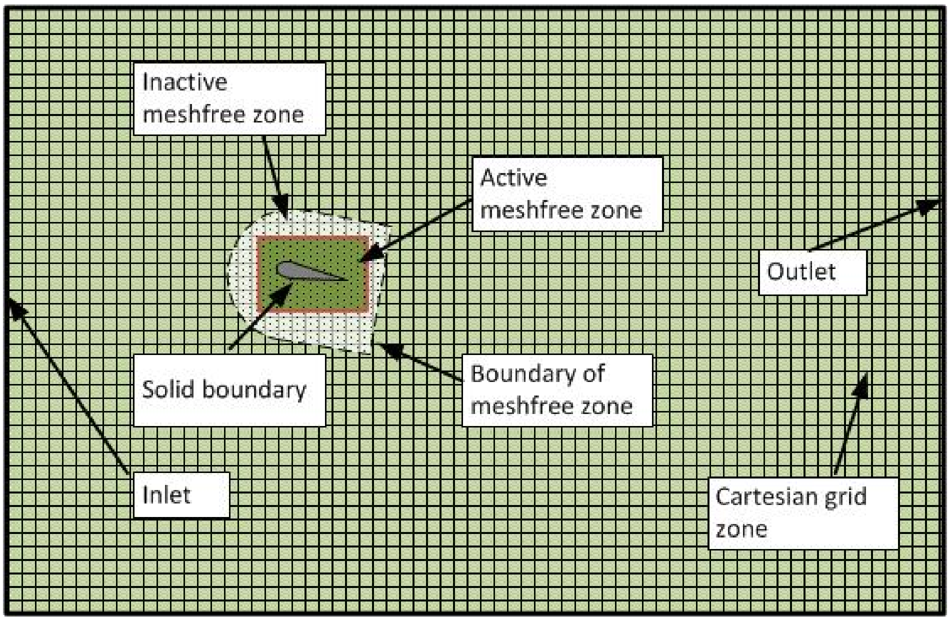

Fig. 1 Hybrid grid configuration in fluid domain

before marching on to the next time step [12]. This deficiency of partitioned methods is overcome by the use of closely coupled systems, in which several inner or sub-iterations of fluid and structure solvers are run, within a single time step, to reach convergence at the interface before moving on to the next time step [14, 20, 12]. In fact, closely coupled systems attempt to improve accuracy and numerical stability in exchange of increased computational cost caused by higher number of computations in each time step.

Another requirement for flow induced vibration problems is to deal with moving boundaries. Traditional mesh based methods (like Finite Element, Finite Volume and Finite Difference), show an inherent limitation in this respect. These methods make use of computational grids which have some sort of pre-defined connectivity amongst the grid nodes. This constraint strongly inhibits the capability of mesh based methods to effectively deal with the moving boundaries. Therefore, use of traditional mesh based methods for FSI problems brings in the cumbersome tasks of extensive re-meshing and data interpolations.

In this paper, a hybrid fluid grid is used to deal with moving solid boundaries encountered in FSI problems in general and flow induced vibration problems in particular. For this purpose, fluid domain is divided into two zones. A boundary fitted meshfree nodal cloud is generated around the solid object. This meshfree cloud moves and morphs with the solid object during its motion. On the outer side, the meshfree cloud is surrounded and partially overlapped by a static Cartesian grid. Schematic of the hybrid fluid grid is shown in Fig. 1. In meshfree zone, space splitting of flow equation is carried out by multiquadric (MQ) Radial Basis Function in Finite Difference mode (RBF-FD). Adaptive shape parameters are used for RBFs, as suggested by [31], to ensure well conditioning coefficient matrices over a grid with variable nodal density. The movement of meshfree nodes is accounted for with Arbitrary-Langrangian-Eulerian (ALE) formulation of N-S equations [28]. This formulation provides an elegant way of solving flow equations over moving data points. A conventional five point differencing is used for spatial derivatives of flow equation in Cartesian zone. Flow equations are solved in their Eulerian form over static Cartesian grid. Elastically supported solid objects are assumed to be rigid with one or two degrees of freedom. The solution scheme provides flexibility to deal with arbitrarily shaped moving objects with the use of meshfree method. Moreover, use of computationally efficient conventional finite differencing helps improve the performance by reducing computation time for each time step.

A closely coupled algorithm is used for interaction between fluid and structural solvers. This has been achieved by performing a sub-iterative predictor-corrector scheme, within each time step, until mutual convergence is reached at fluid-structure interface. In order to reduce the computational overheads during closed coupling procedure, only near field flow domain is used during the sub-iteration

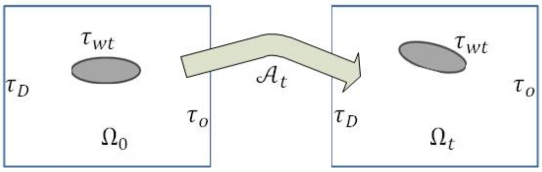

Fig. 2 ALE mapping of reference configuration Ω_0 over current configuration Ω_t

process. Moreover, the novel concept of adaptive sizing of influence domain for RBFs has also been introduced. The concept has been implemented in conjunction with adaptive shape parameters for RBF as suggested by [31]. The aim is to avoid inaccuracies or ill-conditioning effect due to inappropriate number of neighbouring particles or inappropriate value of shape parameter.

This paper is organized as follows: Section 2 outlines the governing fluid and solid equations. It also includes a brief introduction about Radial Basis Functions in Finite Difference Mode (RBF-FD) and space and time splitting for N-S equations. Formulation of the problem including treatment of hybrid fluid grid in fluid domain, adaptive sizing influence domain and FSI coupling algorithm has been described in Section 3. Detail of numerical tests is included in Section 4. Finally, conclusions are drawn in Section 5.

2 Governing equations

2.1 Flow equations

In present work, flow equations, over non-stationary meshfree grid, are dealt with Arbitrary Lagrangian Eulerian (ALE) to account for the nodal movement. The computational domain at initial time t_0 is taken as reference configuration Ω_0 as shown in Fig. 2. At any arbitrary time t reference configuration Ω_0 can be mapped over current configuration Ω_t, as [28]:

$$\mathcal{A}_t : \Omega_0 \rightarrow \Omega_t \tag{1}$$

$$\mathbf{X} \rightarrow x(\mathbf{X}, t) = \mathcal{A}_t(\mathbf{X}) \tag{2}$$

ALE velocity is calculated as $\mathsf{v} = \partial \mathcal{A}_t / \partial t$. Non-dimensionalized pressure-velocity $(\mathbf{P}, \mathbf{u})$ form of time varying, incompressible, viscous flow equations in ALE formulation is given by [53]:

$$\partial_t \mathbf{u} = -\nabla P - (\mathbf{u} - \mathsf{v})).(\nabla \mathbf{u}) + (1/\mathbf{Re})\nabla^2 \mathbf{u} \tag{3}$$

$$\nabla . \mathbf{u} = 0 \tag{4}$$

At each node, ALE velocity is set equal to the velocity of node. For static grid, the nodal velocity v becomes zero and the momentum Eq. (3) transforms to its corresponding Eulerain form. Time discretization of flow equations is carried out using pressure projection method by [7]. This results in an intermediate momentum equation without pressure term. Convective term of this intermediate momentum equation is dealt with Adam-Bashforth scheme while viscous term is treated with Crank-Nicholson scheme as used by [35]. Resulting form of decoupled momentum equation is expressed as:

$$\begin{aligned} \frac{\mathbf{u}^* - \mathbf{u}^n}{\Delta t} = & -\frac{1}{2}\left[3\left(\mathbf{u}^n - \mathsf{v}^n\right).\nabla \mathbf{u}^n - \left(\mathbf{u}^{n-1} - \mathsf{v}^{n-1}\right).\nabla \mathbf{u}^{n-1}\right] \\ & + \frac{1}{2\mathbf{Re}}\left[\nabla^2\left(\mathbf{u}^n + \mathbf{u}^*\right)\right] \end{aligned} \tag{5}$$

$$\frac{\mathbf{u}^{n+1} - \mathbf{u}^*}{\Delta t} = -\nabla P^{n+1} \tag{6}$$

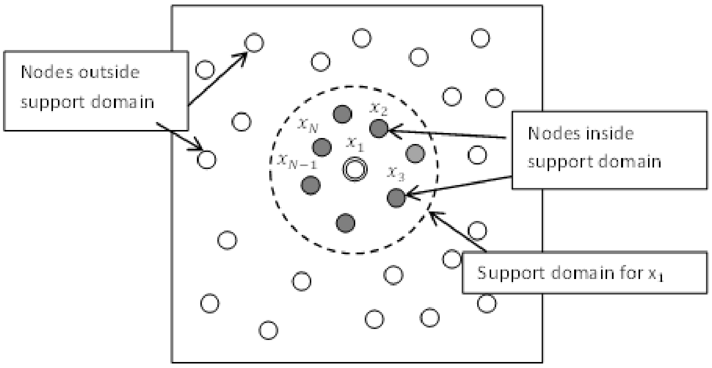

Fig. 3 Support domain of a reference node

In general, the intermediate velocity field $\mathbf{u}^*$ does not satisfy continuity. Therefore, divergence free condition is enforced in projecting step by applying continuity condition from Eq. (4) over velocity field at $\mathbf{u}^{n+1}$ resulting in a pressure Poisson equation given by:

$$\nabla^2 P^{n+1} = (1/\Delta t)\nabla.\mathbf{u}^* \tag{7}$$

At every time step, intermediate velocity field $\mathbf{u}^*$ is calculated by implicitly solving Eq. (5) subject to following condition on boundary τ (as shown in Fig. 2):

$$\mathbf{u}^*|_\tau = \mathbf{u}_\tau + \Delta t \nabla P^n \tag{8}$$

Intermediate velocity field is used to calculate pressure by solving Poisson equation (7). At boundaries τ, Neumann boundary condition is used for pressure as:

$$\mathbf{n}.\nabla P^{n+1}|_\tau = \frac{1}{\Delta t}\left[\mathbf{n}.(\mathbf{u}^* - \mathbf{u}^{n+1})_\tau\right] \tag{9}$$

Where $\mathbf{n}$ is the vector towards outward normal to boundary τ. Finally, velocity field at the end of time step $\mathbf{u}^{n+1}$ is calculated using Eq. (6) with the following velocity boundary conditions:

$$\begin{aligned}
&\textit{at inlet boundary } \tau_D \ \ : && \mathbf{u}^{n+1}|_{\tau_D} = U \\
&\textit{at solid boundary } \tau_{Wt} : && \mathbf{u}|_{\tau_{Wt}} = \mathsf{v}_{\tau_{Wt}} \\
&\textit{at outlet boundary } \tau_o \ \ : && \frac{\mu}{\rho}\left(\frac{\partial \mathbf{u}}{\partial \mathbf{n}}\right)_{\tau_o} = P^{n+1} - P_{ref}
\end{aligned}$$

Spatial derivatives appearing in the flow Eqs. (5) - (9) are treated differently at meshfree and Cartesian nodes. For meshfree nodes, RBF-FD method is used to calculate spatial derivatives over arbitrary data points. The method has been discussed in Section 2.2 in detail. Classical 5-point finite difference stencil is used to approximate spatial derivatives over Cartesian grid. RBF-FD, as well as 5-point central difference scheme yield sparse matrix equations which are solved using Generalized Minimum Residual (GMRES) method [47].

2.2 RBF-FD for flow equations

As mentioned earlier, spatial derivatives appearing in flow equations are treated with local RBFs in finite difference mode (RBF-FD) in meshfree zone. RBF-FD is the generalization of classical finite difference method over set of scattered data points [41]. The idea is to write spatial derivative $\mathcal{L}$ of any field variable u at any point (or node) in the computational domain, say $\mathbf{x}_1$, using the values of same variables at the surrounding nodes as shown in Fig. 3. Using classical finite differencing, this spatial derivative $\mathcal{L}$ can be written as:

$$\mathcal{L}\mathsf{u}(\mathbf{x}_1) = \sum_{j=1}^{N} \mathbf{W}_{1,j}^{(\mathcal{L})} \mathsf{u}(\mathbf{x}_j) \tag{10}$$

where N is the number of nodes in the support domain of node $\mathbf{x}_1$, $\mathsf{u}(\mathbf{x}_j)$ is the value of parameter u at node $\mathbf{x}_j$ and $\mathbf{W}_{1,j}^{(\mathcal{L})}$ is the weight of corresponding differential operator $\mathcal{L}$ at node $\mathbf{x}_j$ for node $\mathbf{x}_1$.

Using standard RBF interpolation, the approximation $s(\mathbf{x})$ to a real valued function $\mathsf{u}(\mathbf{x})$, over a set of distinct points $\mathbf{x}_j \epsilon \mathbf{R}^d, j = 1, 2, ...N$ is given by [60]:

$$\mathsf{u}(\mathbf{x}) \approx s(\mathbf{x}) = \sum_{j=1}^{N} \lambda_j \phi(\|\mathbf{x} - \mathbf{x}_j\|) + \beta \tag{11}$$

where $\phi\left(\|\mathbf{x} - \mathbf{x}_i\|\right)$ is a radial basis function, $\|.\|$ is a standard Euclidean norm and λ_i and β are the expansion coefficients. Multiquadric (MQ) function ($\phi(r) = \sqrt{r^2 + \sigma^2}$, where σ is RBF shape parameter) has been used for current solution scheme. Equation (11) can be written in Lagrange form as:

$$\bar{s}(\mathbf{x}) = \sum_{j=1}^{N} \mathcal{X}\left(\|\mathbf{x} - \mathbf{x}_j\|\right) \mathsf{u}\left(\mathbf{x}_j\right) \tag{12}$$

where $\mathcal{X}\left(\|x - x_j\|\right)$ satisfies the cardinal conditions as

$$\mathcal{X}\left(\|x_k - x_j\|\right) = \begin{cases} 1, \text{ if } k = j \\ 0, \text{ if } k \neq j \end{cases} \qquad k = 1, 2, ...N \tag{13}$$

Applying the differential operator $\mathcal{L}$ on Eq. (12) at node x_1 we have:

$$\mathcal{L}\mathsf{u}\left(x_1\right) \approx \mathcal{L}\bar{s}\left(x_1\right) = \sum_{j=1}^{N} \mathcal{L}\mathcal{X}\left(\|x_1 - x_j\|\right) \mathsf{u}\left(x_j\right) \tag{14}$$

Comparing Eqs. (10) and (14), RBF-FD weights $\mathbf{W}_{1,j}^{(\mathcal{L})}$ can be written as:

$$\mathbf{W}_{1,j}^{(\mathcal{L})} = \mathcal{L}\mathcal{X}\left(\|x_1 - x_j\|\right) \tag{15}$$

In practice, these weights are computed by solving the following linear system [41]:

$$\begin{bmatrix} \Phi & e \\ e^T & 0 \end{bmatrix} \begin{bmatrix} W \\ \mu \end{bmatrix} = \begin{bmatrix} \mathcal{L}\phi_1 \\ 0 \end{bmatrix} \tag{16}$$

where $\Phi_{i,j} = \phi\left(\|x_j - x_i\|\right), i, j = 1, 2, \ldots, N$, $e_i = 1, 2, \ldots, N$, $\mathcal{L}\phi_1$ represents the column vector $\mathcal{L}\phi_1 = \left[\mathcal{L}\phi\|x - x_1\|\mathcal{L}\phi\|x - x_2\| \ldots \mathcal{L}\phi\|x - x_N\|\right]^T$ evaluated at node x_1 and μ is a scalar parameter which enforces the condition:

$$\sum_{j=1}^{N} \mathbf{W}_{1,j}^{(\mathcal{L})} = 0 \tag{17}$$

RBF-FD problem is set up at each meshfree node x_1 to obtain a separate matrix Eq. (16) for each spatial derivative. Evaluation of these equations gives RBF-FD weights $\mathbf{W}_{1,j}^{\mathcal{L}}$ for all the nodes in the support domain of x_1. These weights are then used to calculate the derivatives $\mathcal{L}$ of any field variable u at x_1 using Eq. (10).

2.3 Solid equations

The current solution scheme has been applied for problems relating to flow around spring mounted airfoil and cylindrical objects which are able to vibrate due to fluid forces. Cylindrical objects can perform translatory motion along horizontal and vertical directions as shown in Fig. 4(a). The airfoil is able to vibrate vertically as well as rotate about its elastic axis as depicted in Fig. 4(b). The equations of motion along translational axes (x, y) as well as rotational direction α are as follows:

$$m\ddot{x} + d_x\dot{x} + k_x x = D(t) \tag{18}$$

$$m\ddot{y} + d_y\dot{y} + k_y y = L(t) \tag{19}$$

$$I_\alpha\ddot{\alpha} + d_\alpha\dot{\alpha} + k_\alpha\alpha = M(t) \tag{20}$$

Here m and I_α represent mass and second moment of inertia of the solid respectively. d_x and d_y are the damping constants and k_x, k_y are spring stiffness values along x and y directions respectively. d_α is the rotational damper and k_α is the rotational spring stiffness. $L(t)$, $D(t)$ and $M(t)$ are time dependant lift, drag and moment values.

External forces and moment appearing in Eqs. (18) - (20) can be evaluated by integrating fluid stresses (τ_{ij}) and their corresponding moments about elastic axis over the entire solid surface S. For unit thickness of solid, the fluid forces on solid objects can be expressed as [51]:

$$Drag = D = \int_{\Gamma_{W_t}} \left(\sum_{j=1}^{2} \tau_{1j} n_j \right) dS \tag{21}$$

$$Lift = L = \int_{\Gamma_{W_t}} \left(\sum_{j=1}^{2} \tau_{2j} n_j \right) dS \tag{22}$$

Here, n_i is the component along x_i, of unit vector $\hat{n}$ towards outward normal to the surface $\partial\Omega_t$ on Γ_{W_t}. For airfoil, the moment around its elastic axis is calculated as under:

$$Moment = M = \int_{\Gamma_{W_t}} \left(\sum_{i,j=1}^{2} \tau_{ij} n_j r_i \right) dS \tag{23}$$

Moment arm of force defined as $r_i = -(X_i - X_{EO_i})$, where X_i is the coordinate of point on surface and X_{EO_i} is the coordinate of elastic axis. Differential equations for motion of solid are solved using explicit RK-4 method to get displacements at next time step.

3 Problem formulation

3.1 Hybrid fluid grid arrangement

As mentioned before, the fluid domain is represented by a hybrid grid comprising of meshfree nodal cloud and Cartesian mesh. Schematic of hybrid fluid grid around solid is shown in Fig. 1. The near field flow region, around the solid, is represented by a body conformal meshfree nodal cloud. These meshfree nodes follow the movement of solid boundary during the simulation. In the far field, static Cartesian grid is used which surrounds the meshfree nodal cloud. Moreover, some parts of meshfree cloud are overlapped by surrounding Cartesian mesh. The fluid grid can therefore be divided into following three zones:

1. Cartesian zone: This comprises of Cartesian mesh. Conventional finite difference scheme is here used for spatial discretization of flow equations
2. Active meshfree zone: This zone consists of meshfree nodes which are not overlapped by Cartesian mesh. RBF-FD scheme is used here for evaluation of spatial derivatives.

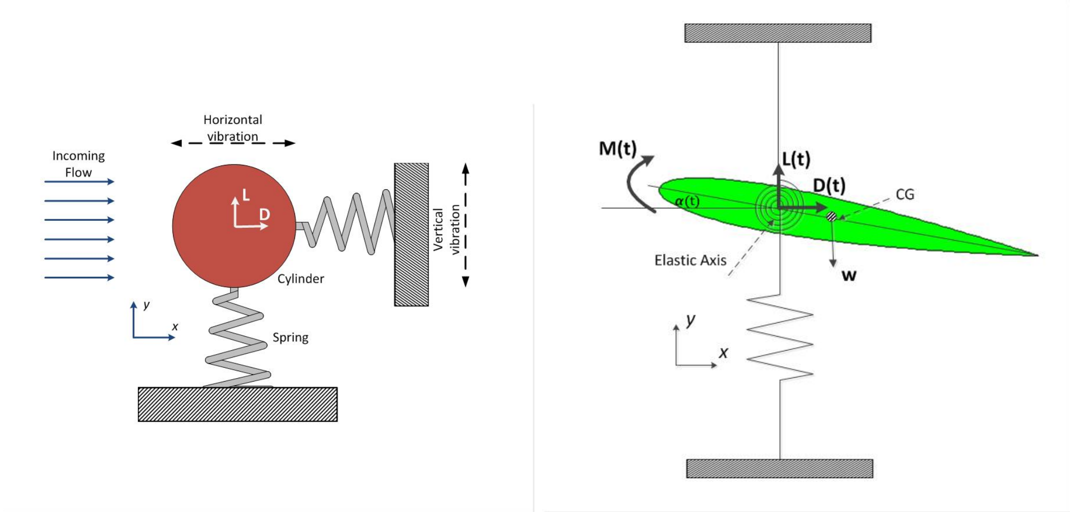

(a) Spring mounted cylinder with two degrees of freedom

(b) Airfoil with two degrees of freedom

Fig. 4 Solid objects in fluid

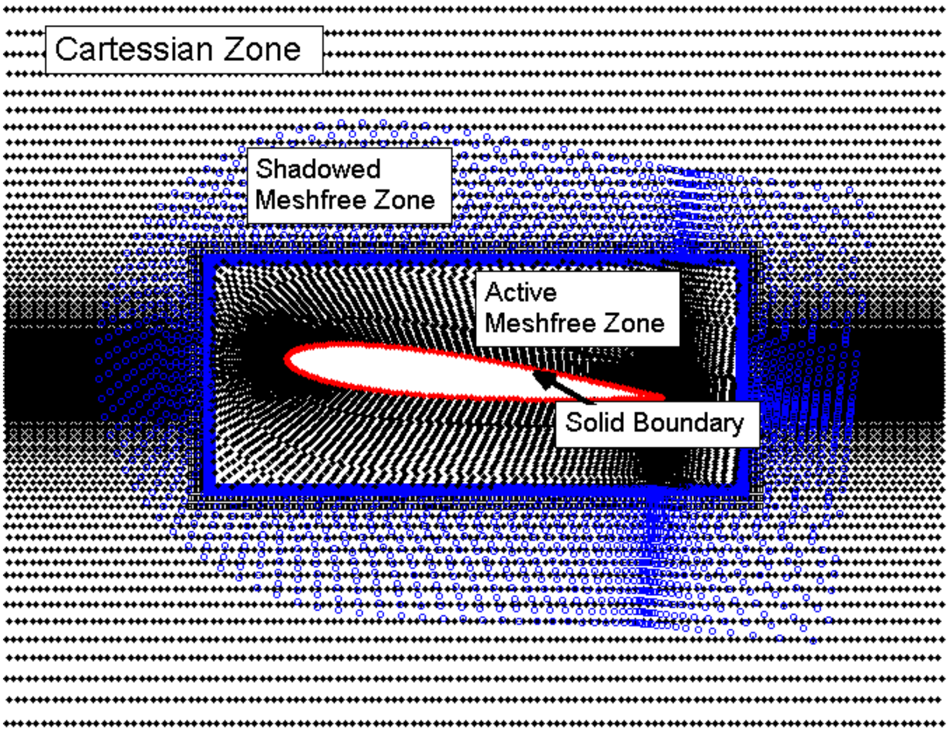

Fig. 5 Hybrid grid around NACA0012 airfoil. Meshfree nodal cloud is surrounded and partially overlapped by Cartesian grid

3. Shadowed (or inactive) meshfree zone: This zone represents the meshfree nodes which are overlapped by Cartesian mesh. This zone is treated as *inactive* and solution is not computed on nodes falling in this zone.

Different zones of typical hybrid grid generated around NACA0012 airfoil are shown in Fig. 5. The computational nodes falling in meshfree and Cartesian zones are treated differently. Therefore, in order to apply respective spatial treatment in meshfree and Cartesian zones, the computational nodes are classified in 5 different categories according to the regions they fall in. This classification of nodes is depicted in Fig. 6. Detail of nodes falling in each category is given below:

- **Category-I nodes**: These are the nodes which lie on Cartesian stencil and are sufficiently away from meshfree zone as shown in Fig. 6. These nodes are stationary and spatial derivatives at these are calculated using five point central difference scheme.
- **Category-II nodes**: These nodes also lie on Cartesian stencil and are treated with central difference scheme. However, they are located close to the meshfree zone and can directly influence the results on neighbouring meshfree nodes. Category-II nodes can therefore fall in the influence domain of nearby meshfree nodes. These nodes are also included in the neighbourhood particle search for meshfree nodes.
- **Category-III nodes**: These nodes fall exactly at the boundary of meshfree-Cartesian zones. Category-III nodes are stationary and aligned with Cartesian stencil. However, these are part of active meshfree zone and are treated with RBF-FD method. Although these are meshfree nodes but they also act as boundary nodes for Cartesian grid. During solution over Cartesian zone, the values of field variables (pressure and velocity values) at category-III nodes are taken as boundary condition.
- **Category-IV nodes**: These nodes fall in *active* meshfree zone. These nodes are part of moving grid which are treated with RBF-FD method and ALE formulation of N-S equations.
- **Category-V nodes**: These are the nodes which fall in *inactive* meshfree zone. These are part of meshfree grid but are *overshadowed* by superimposing Cartesian grid. The nodes are therefore treated as *inactive* and do not participate in current time step computations.

A summary of different categories of nodes and their computational treatment is given in Table 1. During the simulation, the two way exchange of data between Cartesian and meshfree zones takes place in the following manner:

- Information from meshfree to Cartesian grid is transferred through Category-III nodes. These nodes are treated with RBF-FD method. However, they are static and fall exactly on Cartesian stencil. Therefore, these nodes can act as boundary nodes for Cartesian grid. During simulation process, the most updated values of field parameters (pressure and velocity values) at Category-III nodes are taken as Dirichlet boundary conditions for surrounding Cartesian nodes.
- Transfer of data from Cartesian to meshfree zone takes place through Category-II nodes. These nodes fall in the influence domain of neighbouring meshfree nodes. Therefore, the flow parameters at Category-II nodes affect the derivative approximations at respective meshfree nodes through corresponding RBF weights. As a result, flow parameters values at meshfree nodes are influenced by the results at Category-II nodes.

During simulation, the movement of solid is accommodated, in fluid, by allowing Category-IV and V nodes to follow the motion of solid boundary. During this process, Category-I, II and III nodes remain stationary. Fig. 7 shows the movement of meshfree grid surrounded by static Cartesian grid between time instance t_0 to t_1. In this case, meshfree cloud is rotating in *counter-clockwise* direction. As meshfree zone is rotated, some inactive (category-V) nodes may come out of the *shadowed* region and appear in the active meshfree zone. Some of these nodes are shown as group-A in Fig. 7. As these category-V nodes reach the active meshfree zone, their category is changed and these are put in category-IV. This means that these nodes will participate in future computations. However, in order to set these *newly activated* nodes for next time step calculations, field parameter (pressure and velocity) values are assigned by interpolating the data from surrounding nodes. For this purpose, an RBF type interpolation is set up at each *newly activated* node. Values of field parameters are interpolated at these nodes using corresponding values from surrounding nodes. During this movement of meshfree grid, some category-IV nodes will also be pushed behind the Cartesian grid (for example group-B nodes shown in Fig. 7). These nodes are recategorized as Category-V nodes and therefore, do not participate in further calculations unless they reappear in the active meshfree zone later.

The above mentioned treatment of moving boundary needs only meshfree grid to move and accommodate the motion of solid. As a result, the number and location of nodes in Cartesian zone do not change during the simulation. This has a computational advantage as the matrices for solving Eqs. (5) and (6), in Cartesian zone, remain unchanged. These matrices are required to be formulated only once at the start of iteration process. Therefore, during the simulation, matrix equations for solving

Eqs. (5) and (6), are needed to be updated in meshfree zone only as the number and location of active meshfree nodes changes continuously.

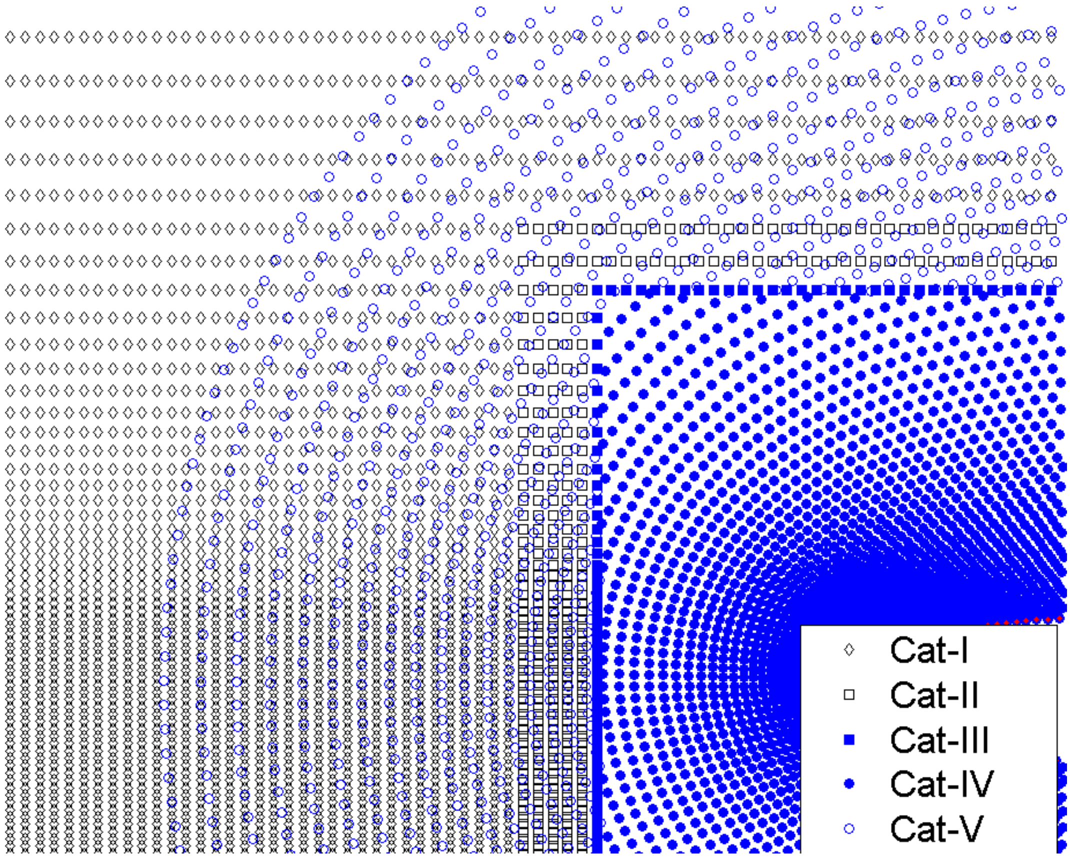

Fig. 6 Classification of computational nodes in hybrid fluid grid

Table 1 Categorization of computational nodes in hybrid grid

Category	Zone	Method	Stationary / Moving	Remarks
Cat-I	Cartesian	FD	Stationary	
Cat-II	Cartesian	FD	Stationary	Fall in the influence domain of neighbouring mesfhree particles
Cat-III	Meshfree	RBF-FD	Stationary	Act as boundary particles for Cartesian grid
Cat-IV	Meshfree	RBF-FD	Moving	Active meshfree nodes
Cat-V	Meshfree	RBF-FD	Moving	Inactive meshfree nodes

3.2 Adaptive sizing of influence domain for RBF

Accuracy of RBF based schemes largely depends on the well conditioning of interpolation matrix [33]. In fact, condition number of interpolation matrix for RBFs grows with increasing the number of computational nodes participating in derivative approximation at a certain point [49]. Larger number of particles, participating in RBF interpolation, will also require more number of arithmetic operations

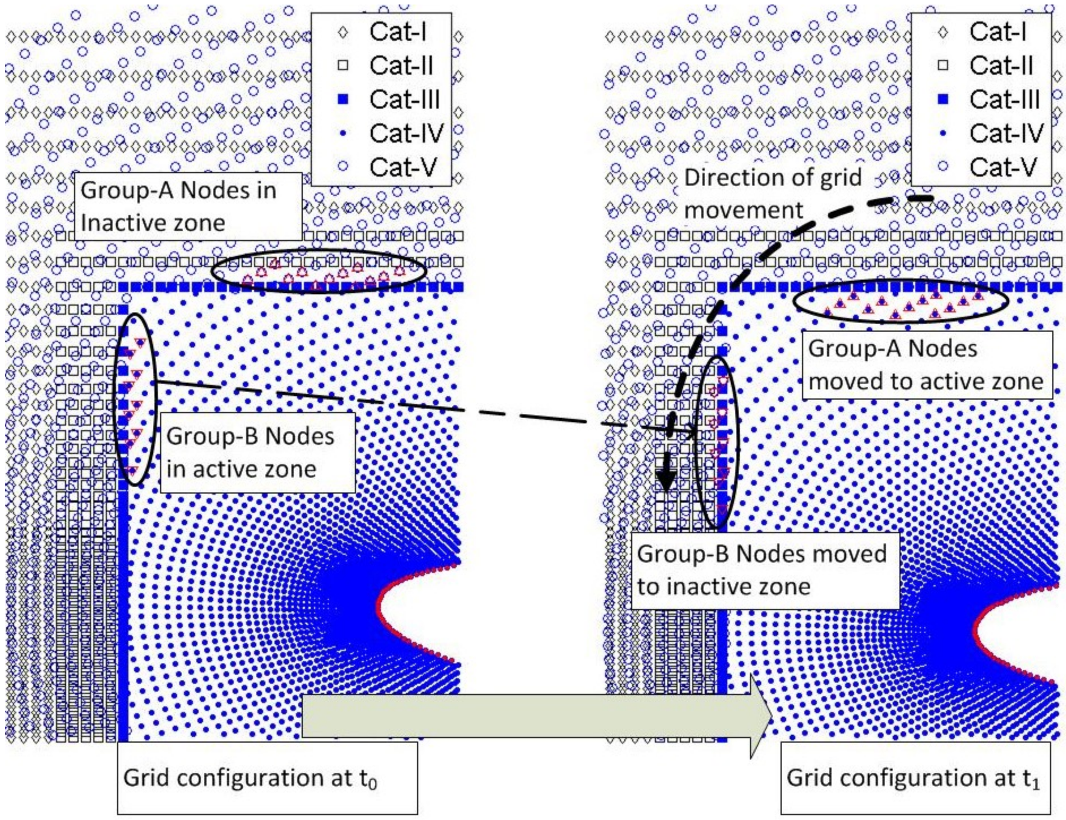

Fig. 7 Activation and deactivation of meshfree nodes during movement of meshfree grid

for single derivative approximation. Therefore in local RBF, the solution process tends to be computationally intensive with more number of neighbouring particles taking part in derivative approximation at point of interest. At the same time, requirement of sufficient number of collocation data points in the influence domain to ensure accurate derivative approximation using local RBF [12] cannot be subdued. It is therefore important to keep suitable number of particles in the influence domain of every computational node. In practice, this is achieved by specifying size of the influence domain. However, for the set of problems considered here, the grid resolution changes significantly to accurately capture flow parameters near the airfoil surface. Therefore, a constant domain size, for all the nodes, will either place too many neighbouring particles in the influence domains of nodes closer to the airfoil or there will be too less neighbouring particles around nodes in low nodal density region. In order to overcome this problem, adaptive sizing of influence domain has been introduced. For this purpose, the size of influence (or neighbourhood) domain for each node is decided based on the nodal density around it. An iterative algorithm is used to calculate the radius of influence domain around every node which ensures 25 to 35 neighbouring particles. The aim is to make sure that every node has enough number of neighbouring particles to calculate spatial derivatives using local RBF and at the same time influence domain is not too dense to render the interpolation matrix ill-conditioned or the process inefficient. Adaptive domain sizing applied to a typical grid around NACA0012 airfoil is shown in Fig. 8. The domain size progressively becomes larger as we go away from the airfoil to accommodate required number of neighbouring particles in coarser grid zones.

Fig. 9(a) shows variation in number of neighbouring particles for fixed and adaptive domain sizes. Improvement in condition number of coefficient matrices with adaptive sizing can be seen in Fig. 9(b) which plots condition number of RBF matrices, against coordinate location x, for both fixed and adaptive domain sizing applied to 1-dimensional, non-uniform particle distribution. With increasing nodal density, total number of neighbouring particles increases for fixed domain sizing. This results in enormously high condition number in refined grid region. On the contrary, adaptive domain sizing

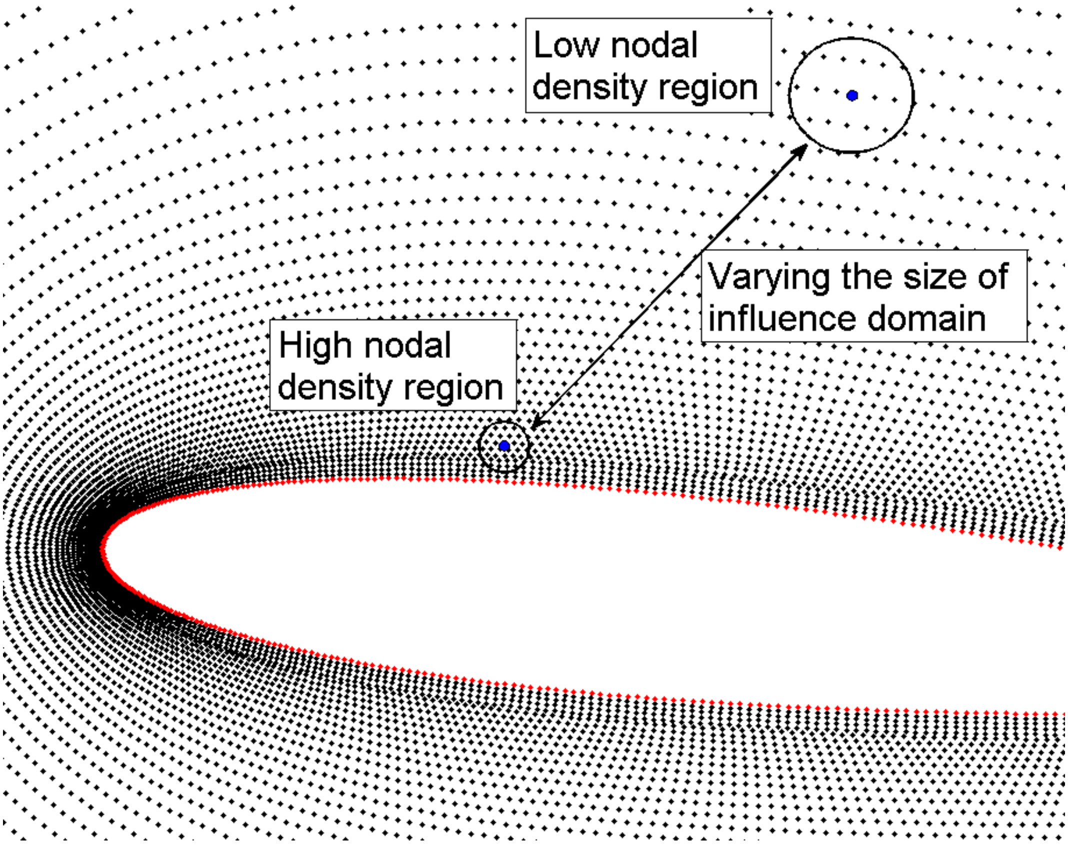

Fig. 8 Adaptive sizing of influence domain applied to grid around NACA0012 airfoil

ensures only the required number of neighbouring particles thus maintaining well conditioned matrices all over the domain.

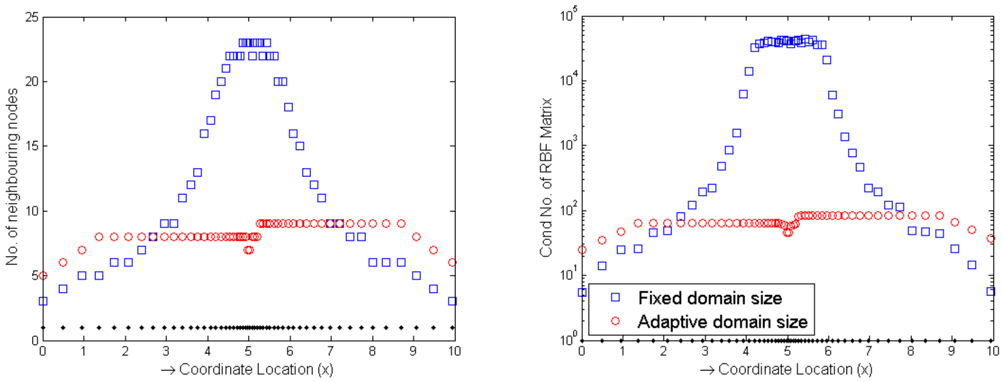

(a) Variation in number of neighbouring particles (b) Variation of Condition Number

Fig. 9 Fixed and Adaptive sizing applied to 1-dimensional non-uniform particle distribution

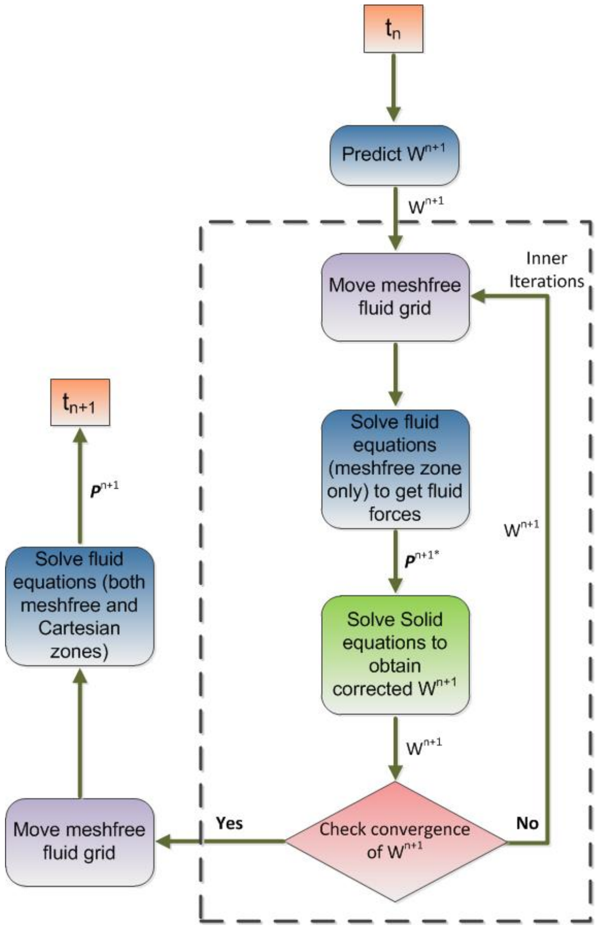

Fig. 10 Flow chart of solution scheme at a single time step

3.3 FSI coupling algorithm

A closely coupled model has been used to transfer data between fluid and structural solvers. Close coupling has been achieved by iteratively running fluid and structural solvers at a single time step. During this process, exchange of fluid and structural data (fluid forces and structural deformations) takes place at solid boundary. The sub-iteration process continues until convergence is reached between results of fluid and structural solver. Closely coupled FSI models are often criticized for their complexity and inefficiency [21] caused by increased number of computations during sub-iterations. The high computational cost is primarily caused by repeated flow solutions at a single time step. It is however understood that the very purpose of obtaining these repeated solutions is to get fluid forces at fluid-structure interface which could then be used to calculate structural deformations. Flow parameters at far field show minimal variation when the results are being *fine tuned* at solid boundary during sub-iterations. It is therefore logical to include only near field fluid for iterative refinement of fluid forces at solid boundary. In view of this, only meshfree zone is included in sub-iteration calculations of fluid solver. In fact, Cartesian grid zone is included in computation only during outer (time step) iteration marching of fluid domain. During sub iterations, the results are updated only over the meshfree zone to get fluid forces as shown in the flow chart of solution scheme at a single time step in Fig. 10. The coupling algorithm of the two field solution during FSI marching is shown in Fig. 11 and is carried out in following manner:

1. Structural displacement W^{n+1} is predicted at time t^{n+1} using velocity and acceleration of previous time step t^n.
2. Predicted structural displacement is mapped over the fluid grid.

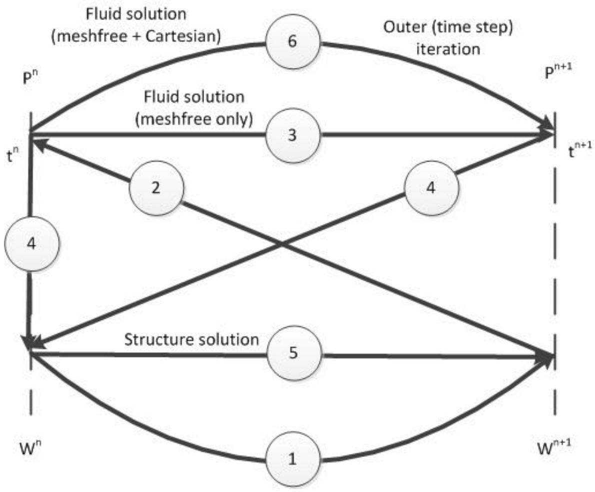

Fig. 11 Coupling algorithm of two field solution (P^n and W^n represent fluid forces and solid deformation respectively, at n^{th} iteration)

3. Mesfhree fluid grid is displaced according to predicted structure displacement and fluid equations are solved only in meshfree zone. The fluid forces P^{n+1*} are thus calculated, at solid surface, using flow parameters.
4. An average of fluid forces P^{n+1*} and P^n is mapped over structural grid to get applied loads.
5. Solid equations are solved using averaged fluid forces to get the corrected structural deflection W^{n+1}. At this stage, corrected structural deflections are compared with previously obtained values.
6. Process from step 2 to 5 is repeated until the resultant structural deflection values achieve desired convergence level. Outer iteration is then run in which both Cartesian and meshfree fluid zones participate to march to next time step t^{n+1} and get P^{n+1}.

It is understood that exclusion of Cartesian grid for inner iterations may cause some inaccuracies. However, the effect of using reduced fluid domain for inner iterations was found to be minimal during numerical tests. It is also pertinent to highlight that suggested closed coupling scheme is anyway more accurate than corresponding loose coupling which do not attempt to converge the two field solution before marching to next time step.

4 Numerical tests

4.1 Order of convergence over 2-D Domain

This section deals with convergence and accuracy tests for 2-D incompressible N-S equations (Eqs. (3) and (4)) over rectangular domain with hybrid grid. Spatial and temporal accuracy of fluid solver is studied, over hybrid grid, by simulating decaying vortex case. The analytical expression of flow velocity and pressure are known for this problem. Therefore, the test is often used to validate numerical solution schemes [6,35,34]. Followings are the theoretical expressions for time varying pressure and velocity fields $(p(x,y,t),u(x,y,t),v(x,y,t))$:

$$u(x,y,t) = -\cos(\pi x)\sin(\pi y)\exp\left[-(\pi^2 t)/Re\right] \tag{24}$$

$$v(x,y,t) = \sin(\pi x)\cos(\pi y)\exp\left[-(\pi^2 t)/Re\right] \tag{25}$$

$$p(x,t) = -\frac{1}{4}\left[\cos(2\pi x) + \sin(2\pi y)\right]\exp\left[-4(\pi^2 t)/Re\right] \tag{26}$$

Flow Reynolds number is defined as $Re = UL/\nu$, where ν is the kinematic viscosity of fluid, U is the maximum initial velocity and L is the vortex length. Rectangular domain is used with dimensions

$-0.5 \le x \le 0.5$ and $-0.5 \le y \le 0.5$. Central region, spanning $-0.1 \le x \le 0.1$ and $-0.1 \le y \le 0.1$, is set as meshfree zone and remaining region is meshed with Cartesian grid. Tests are run for both static and moving meshfree nodes at $Re = 10$. Static tests are run for uniform as well as random meshfree grid. Randomness is introduced in mesfhree nodes by disturbing their position from corresponding locations on a uniform lattice using a random function of the order of $0.4dx$. Fig. 12 shows the hybrid mesh with space step $dx = 0.1$ and randomized meshfree nodes.

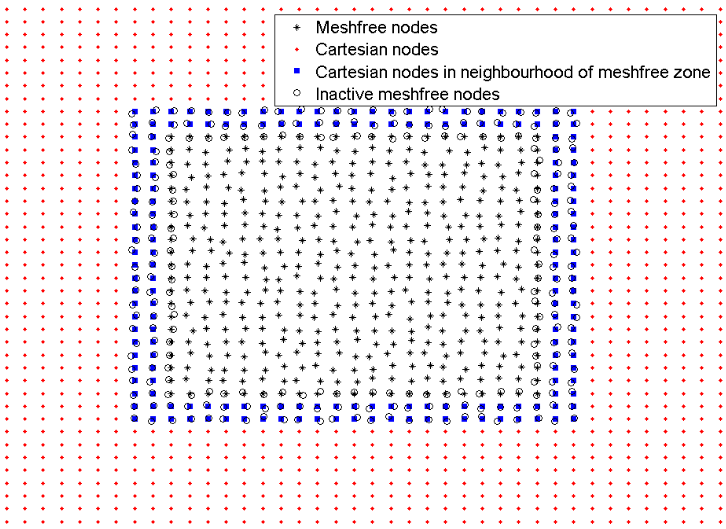

Fig. 12 Hybrid grid in rectangular domain with randomized meshfree particles

For each test case, initial and boundary conditions are introduced using pressure and velocity values obtained from Eqs. (24) - (26) at given time and spatial coordinates (t, x, y). For uniform-static meshfree grid, a separate case is run in which Neumann boundary conditions are used for pressure. For this purpose, pressure values are obtained, at boundary, from velocity field using Eq. (9).

In order to study spatial order of convergence, static test cases are run for time step value of 10^{-5} and for varying grid sizes. Time step value has been kept small to minimize temporal errors. The solutions at $t = 0.5$ are compared with true solutions (using (Eqs 24) - (26)) to get RMS (root mean square) and maximum error values over the entire domain. Logarithmic values of error ($Log_{10}(e)$) are plotted against logarithms of space step ($Log_{10}(dx)$) in Fig. 13(a). Similarly, temporal convergence is studied by keeping grid size constant at $dx = 0.005$ and changing the time step values. Plots of $Log_{10}(e)$ versus $Log_{10}(dt)$ are shown in Fig. 13(b). Order of convergence is defined as the slope of linear curve obtained by least square fit on RMS error data. Values of order of convergence for all cases are summarized in Table 2. It can be observed that spatial order of convergence for both velocity and pressure remains close to 2.5. Order of convergence in time is found to be around 1.0 for both pressure and velocity field with known pressure boundary conditions. Use of Neumann boundary conditions however tends to increase the convergence rate especially for the pressure field.

Moving grid cases are run by making the mesfhree grid rotate about its centre with a variable angular velocity. Angular orientation ($\Theta(t)$) of meshfree grid is defined as $\Theta(t) = \mathbf{A}[1 - \cos(\pi t/2)]$. Value of parameter $\mathbf{A}$ is set to control angular speed and total grid rotation in a given time. Grid configuration at initial time t_0 and at later time $t_1 = 0.5$ are shown in Fig. 14 for $\mathbf{A} = 0.3\pi$. Moving grid tests are run for different values of $\mathbf{A}$ to get different nodal velocities. Space step is set as 0.005 and time step is kept as 10^{-4}. Error values are obtained at $t = 0.5$ by comparing the solutions with true values. Logarithmic (log_{10}) values of RMS and maximum error are plotted against the changing grid speeds in Fig. 15. On the plot, the point at $\mathbf{A} = 0$ corresponds to static grid case. For moving grid, the error values tend to increase with increasing grid speeds and are higher compared with static

Table 2 Spatial order of convergence for static tests

Distribution of mesfhree nodes	Pressure boundary conditions	Spatial / Time	Order of convergence	
			u-velocity	pressure
Uniform	known (using Eq. (26))	Spatial	2.56	2.7
Uniform	Neumann	Spatial	2.59	2.49
Random	known (using Eq. (26))	Spatial	2.66	2.58
Uniform	known (using Eq. (26))	Time	0.99	0.9135
Uniform	Neumann	Time	1.22	1.8

grid. However, slope of the error curve reduces at higher speeds making error to stabilize and not to increase with further increase in grid velocities.

During motion of mesfhree cloud, *grid update* calculations are required to be carried out continuously during the simulation. *Grid update* includes re-categorization of meshfree nodes according to their current location (in active or inactive zone), reallocation of neighbouring particles and recalculation of RBF weights. *Grid update* is particularly important for nodes located close to meshfree-Cartesian zone interface. However, this process requires extensive computational resources (in terms of computer memory and time) and is not considered viable after every iteration. Instead *grid update* can be performed after the grid has been displaced by a certain distance Δd_{update}. Grid movement can be monitored by motion of a *reference node* to find out when *grid update* is necessary. For current test cases, the node at bottom left corner of meshfree zone is considered as *reference node*. During simulation, displacement of a this node is continuously monitored and *grid update* calculations are performed when the *reference node* has been displaced by distance Δd_{update}. In order to determine the effect of *grid update distance* on accuracy of solution, moving grid case with $\mathbf{A} = 0.3\pi$ is run for two different values of *grid update distance*. First case is run for $\Delta d_{update} = 0.5dx$ and second test is run for $\Delta d_{update} = 0.05dx$, where dx is the space step. Time profiles of RMS error for pressure values are shown in Fig. 16. A reference case is also run in which grid was updated after every iteration. RMS error profile for reference is also co-plotted as dotted line. For $\Delta d_{update} = 0.05dx$ and $\Delta d_{update} = 0.5dx$, each grid update is followed by a spike in the error profile. These spikes are caused by variation in RBF weights for calculating spatial derivatives. The spikes are more pronounced for larger *grid update distance*. When the grid is updated less frequently during simulation (as in case of larger *grid update distance*), RBF weight values experience larger variation after update and resulting spikes are more pronounced. A reasonable value of *grid update distance* is therefore necessary as very high spike can even lead to instabilities. However, as long as *grid update distance* is kept within reasonable range, changing its value is not found to significantly affect time averaged error values.

4.2 Flow around cylinders

The solution scheme has been used for flow around cylindrical objects. Three different cases have been considered based on degree of freedom for solid motion. These include flow around stationary solids, flow around solid with one degree of freedom and flow around solid with two degrees of freedom. Flow Reynolds number is defined as $Re = \rho UD/\mu$, Where ρ is the fluid density, U is the free stream velocity, D is the diameter of the cylinder and μ is the dynamic viscosity of the fluid. Reynolds number is kept below 200 in all the cases involving flow around cylinder. The detail of each case is described below.

4.2.1 Flow around static cylinder

The purpose of running static cylinder cases is to establish the accuracy of presented solution scheme before moving on to flow induced vibration cases. Incompressible flow problem around stationary cylinder is studied at a range of Reynolds numbers. For these problems, flow remains steady at low Reynolds numbers ($Re < 49$). However, the flow becomes unsteady due to generation of an oscillating vortex street (known as Kamran Vortex) which appears behind the cylinder at Reynolds numbers from 49 to 200. The problem has extensively been studied previously and sufficient reliable data is available in literature [23, 2, 24, 56, 6, 17] to compare and validate the presented scheme. For present work, a rectangular fluid domain is chosen with dimensions $38D \times 12D$. Center of the cylinder is

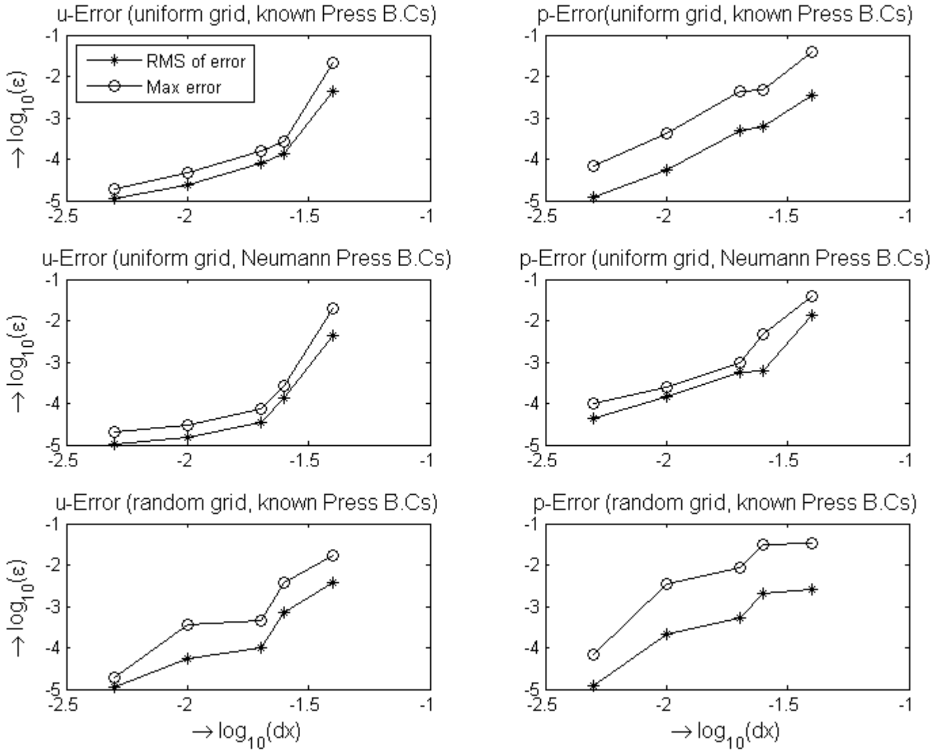

(a) Spatial convergence

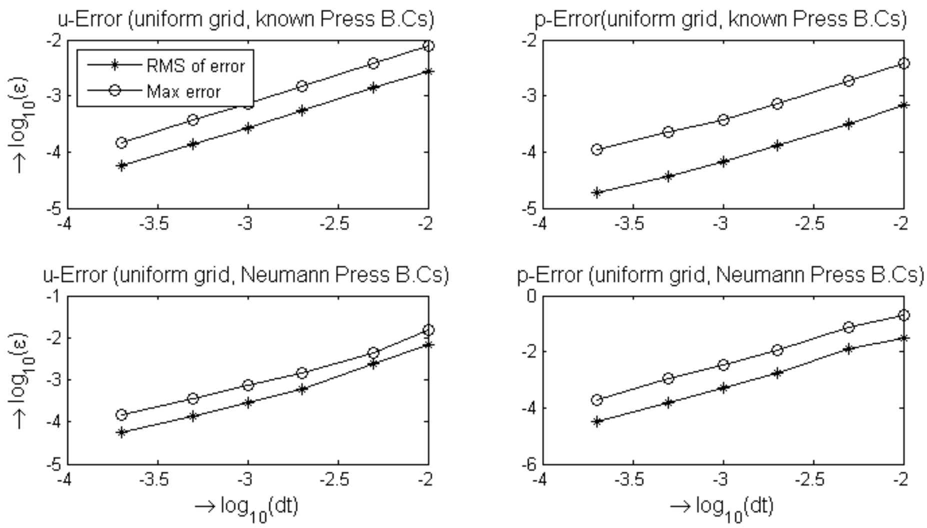

(b) Temporal convergence

Fig. 13 Error Plots for static test case at t=0.5 (*-RMS error, o-Max error)

located at a distance of $8D$ from inlet and $6D$ from each of the side walls. This ensures that the flow remains unaffected by any non-physical disturbances at domain boundary. Meshfree cloud spans $3D \times 3D$ around the cylinder. Remaining fluid domain is meshed with a Cartesian grid. Therefore, meshfree zone constitutes only 1.35 percent of the total domain area. Boundary conditions are applied as mentioned in Section 2.1.

In meshfree zone, nodes are arranged radially around the cylinder. A total of 140 nodes are placed at solid boundary. In order to implement Neumann pressure boundary conditions at solid surface,

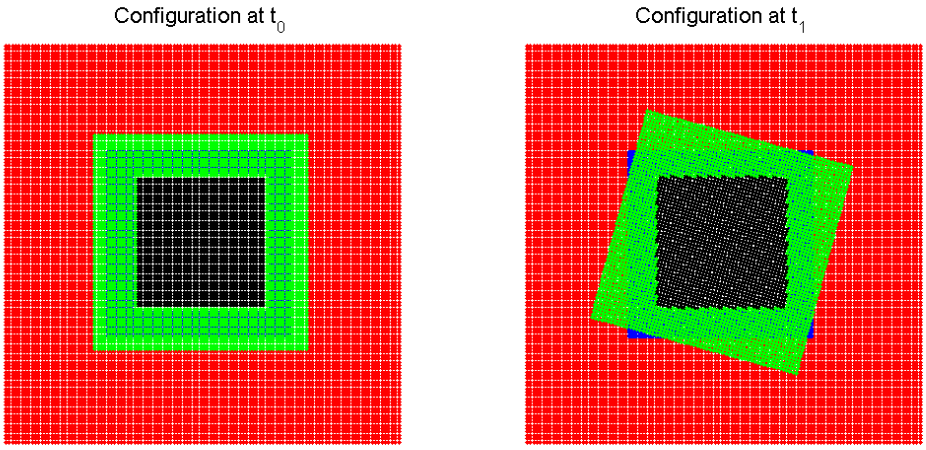

Fig. 14 Grid configuration at initial time $t_0 = 0$ and at time $t_1 = 0.5$ for $\Theta = 0.3\pi[1 - \cos(\pi t/2)]$

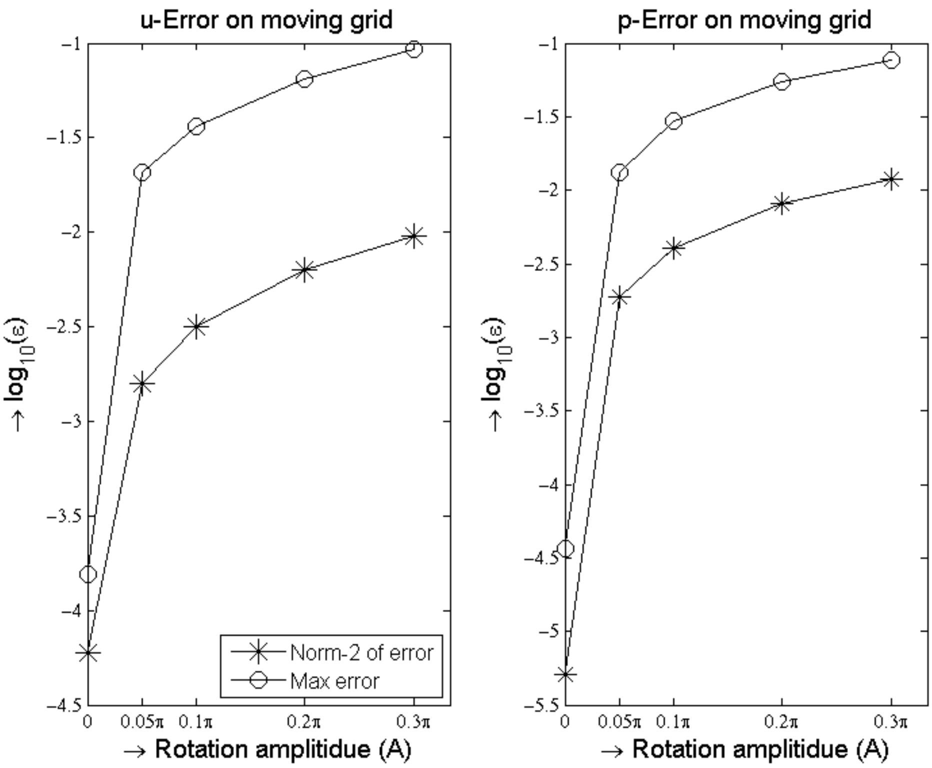

Fig. 15 Error Plots at different angular speed moving meshfree grid at t=0.5 (*-RMS error, o-Max error)

orthogonal nodal arrangement is ensured at least in two nodal layers immediately after the solid boundary. For the static case, meshfree zone will remain stationary during simulation. Therefore, overlapping meshfree zone is not required here (though presence of overlapped inactive meshfree nodes will not make any difference). There are total of 4122 meshfree nodes and 21500 Cartesian nodes in the hybrid grid. Fig. 17(a) shows part of grid close to solid boundary indicating arrangement of meshfree nodes around cylinder. Time step is kept as 5×10^{-3} sec. Lift and drag forces (F_L and F_D) are calculated by integrating vertical and horizontal components of normal and shear stresses at the solid boundary using Eq. (21). The lift and drag coefficients (CD and CL) are then evaluated using following expressions:

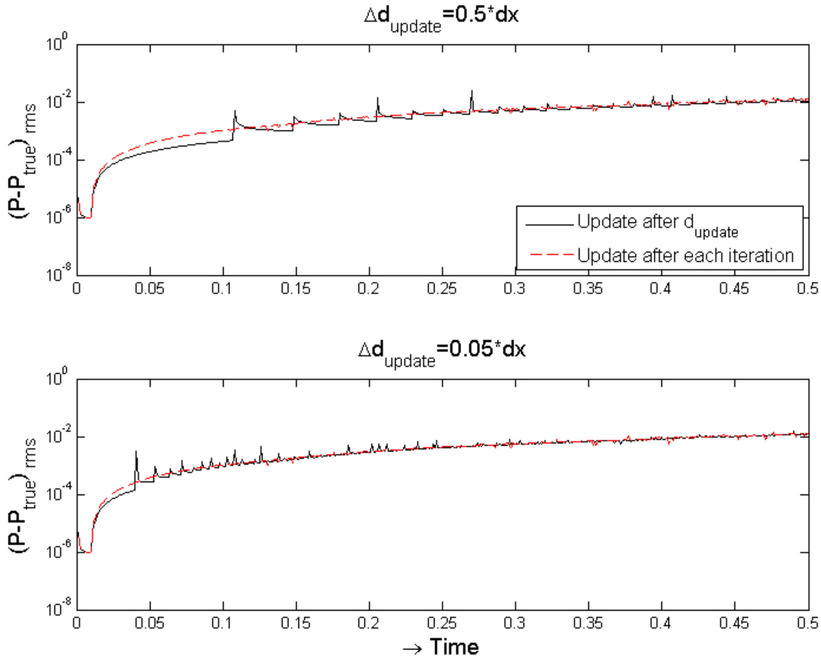

Fig. 16 Time profiles of RMS error for pressure values at different *grid update distance* Δd_{update}

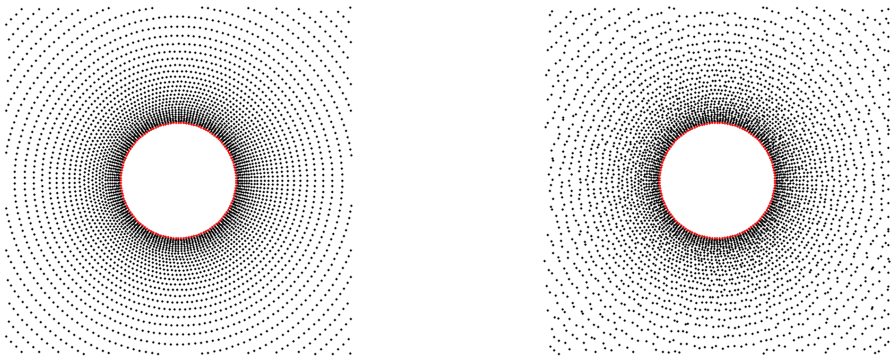

(a) *Ordered* arrangement

(b) *Random* arrangement

Fig. 17 Arrangement of meshfree nodes around circular solid

$$Lift\ coefficient\ = C_L = \frac{F_L}{\rho U^2 D} \tag{27}$$

$$Drag\ coefficient\ = C_D = \frac{F_D}{\rho U^2 D} \tag{28}$$

The solutions are obtained at $Re = 10,\ 20,\ 40,\ 100$ and 200. At $Re = 10,\ 20$ and 40, the flow remains steady behind the cylinder. Resultant value drag coefficient CD, separation angle (θ_{sep}) and length of recirculation region (L_{sep}) are shown in Table 3 along with the results from previous researches [16,52,56] at each Reynolds number. Results from present work show good agreement with previous solutions.

Table 3 Solution parameters (separation angle θ_{sep}, length of recirculation region L_{sep} and drag coefficient C_D) for steady flow around static cylinder at Re =10, 20 and 40

Re	10			20			40		
Source	θ_{sep}	L_{sep}	C_D	θ_{sep}	L_{sep}	C_D	θ_{sep}	L_{sep}	C_D
Dennis[16]	29.6	0.265	2.85	43.7	0.94	2.05	53.8	2.35	1.52
Takami[52]	29.3	0.249	2.80	43.7	0.935	2.01	53.6	2.32	1.54
Tuann[56]	29.7	0.25	3.18	44.1	0.9	2.25	54.8	2.10	1.68
Present case	28.6	0.280	3.09	44.1	0.95	2.19	53.13	2.18	1.63

Table 4 Solution parameters (lift coefficient C_L, drag coefficient C_D and Strouhal number S_t) for unsteady flow around static cylinder at Re =100 and 200

Re	100			200		
Source	C_L	C_D	S_t	C_L	C_D	S_t
Braza[2]	±0.25	1.364±0.015	0.16	±0.75	1.40±0.05	0.2
Ding[17]	±0.28	1.32±0.008	0.164	±0.60	1.327±0.045	0.196
Liu[37]	±0.34	1.35±0.012	0.164	±0.69	1.31±0.049	0.192
Present case	±0.32	1.314±0.009	0.164	±0.62	1.302±0.039	0.194

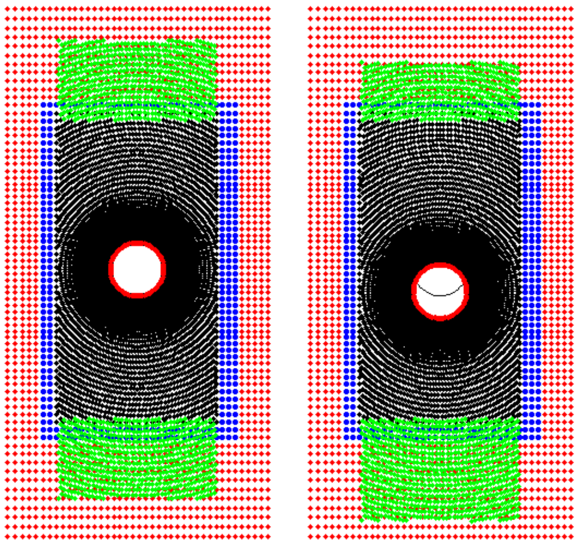

(a) Cylinder at mean position (b) Cylinder below the mean position

Fig. 18 Meshfree cloud movement around vertically vibrating cylinder

Unsteady flow cases are run at $Re = 100$ and 200. Oscillating flow vortices at these flow conditions result in time varying profiles of lift and drag forces at constant frequencies. Lift and drag coefficients as well as Strouhal number ($St = fD/U$, where f is vortex shedding frequency) of flow at these Reynolds numbers are shown in Table 4.

4.2.2 Vortex induced vibration of cylinder with 1-DoF

Vortex induced vibration of an elastically mounted cylinder is studied here. The cylinder has one degree of freedom in cross flow direction. This basic test case of fluid-structure interface is amongst the most revealing problems pertaining to bluff bodies. Simple geometry and well established results available in literature make it an attractive choice to test current FSI solution scheme. Schematic of the problem is the same as Fig. 4(a) except that horizontal degree of freedom is removed. For present work, dimensions of fluid domain are the same as for static case. The dimensions of meshfree zone are however increased in vertical direction and are set as $3D \times 9D$. Dimensions of active meshfree zone are $3D \times 6D$. Vertical dimension of meshfree zone is elongated to allow cross-flow vibration. The solutions are sought on *ordered* as well as *randomized* meshfree nodal arrangement. Randomization is obtained by randomly disturbing the position of meshfree nodes from their corresponding location on the *ordered* grid. For this purpose, a random function of the order of $0.4\Delta r$ (Δr is the radial spacing of nodes) is used. Fig. 17(b) shows a *randomized* nodal arrangement around the cylinder.

During the simulation, solid cylinder vibrates in cross flow direction due to oscillating fluid forces. The meshfree nodal cloud follows the motion of cylinder. In this process, meshfree nodes near top and bottom sides of cloud appear and disappear behind overlapping Cartesian zone. For example, the states of meshfree cloud at two different vertical positions are compared in Fig. 18. As the cylinder goes down, most of the overlapping zone is exposed at the top side and reverse happens at the lower side. Therefore, the activation status of these nodes is continuously updated during the simulation.

The solutions are obtained at flow Re=100. At this Reynolds number, oscillating flow vortices behind the cylinder will produce time varying lift profile. The cylinder is thus able to vibrate vertically under the influence of these forces. Flow induced cylindrical vibrations in cross flow are termed as *self-limiting* phenomenon by [39]. This means that the vibration amplitudes retain their constant value after initial settling down period. Vibration of solid causes reduction in lift force and renders some additional frequency components in fluid force profiles which tend to limit the vibrating amplitudes to specific level [46]. A parameter called *effective elasticity* k^*_{eff} is often used to characterize the system response for such problems. *Effective elasticity* combines the effect of system mass m, stiffness k and reduced vortex shedding frequency $f^* = fU/D$ through the following expression [50]:

$$k^*_{eff} = k - 4\pi^2 m f^{*2} \tag{29}$$

Effective elasticity therefore offers an inclusive representation of system parameters. Mass of the cylinder is set as 3. The solutions are obtained by changing the values of spring stiffness k. Time step value is set as 5×10^{-3}. For every test case, k^*_{eff} is calculated using spring stiffness k and resulting reduced frequency of vortex shedding f^*. Corresponding values of non-dimensionalized vibration amplitudes (Y_{max}/D), maximum lift coefficient ($C_{L_{max}}$) and reduced frequency (f^*) are plotted in Fig. 19. The results are comparable to those obtained by Sheils et al. [50]. Moreover, the results from *ordered* as well as *randomized* meshfree nodal distribution match very closely with each other. This indicates that the solutions are not affected by randomization of meshfree nodes. Plots in Fig. 19(a) indicate a high amplitude region between $0 \leq k^*_{eff} \leq 4$. The lift and drag values are also higher in this range as shown in Figures 19(c) and 19(d). This high amplitude zone is called 'lock-in' zone. In that, the vortex shedding frequency deviates from its original value and equalizes with natural frequency of vibrating system creating resonance. This synchronization of fluid forces with vibrating system results in higher amplitudes. Fig. 19(b) clearly indicates deviation of vortex frequency in 'lock-in' zone. Beyond 'lock-in' zone, a sharp decline in vibration amplitudes is observed. Fig. 20 shows the difference in flow patterns around the cylinder for 'locked-in' and 'un-locked' configurations. Due to high vibration amplitudes in 'lock-in' zone, vortices are stretched and two distinct rows of vortices are formed behind the cylinder. In 'un-locked' zone, the vortex street resumes its conventional form. However, the vortices are being shed in 2S mode in both configurations and 2P mode of vortex shedding is not observed with change in k^*_{eff}. This observation is in line with what was obtained by Placzek et al. [46]. Placzek [46] argues that mode switch from 2S to 2P is only experienced at high Reynolds number which is not the case here.

Above calculations are carried out using closely coupled FSI with reduced fluid domain as mentioned in Section 3.3. In order to compare the accuracy, time profiles of displacement, lift and drag from solution obtained with loosely coupled FSI and closely coupled FSI with reduced as well as full fluid domain are plotted together in Fig. 21. Solutions are obtained on *ordered* meshfree nodes and correspond to the case with $k^*_{eff} = 0.623$. Here, we consider that the closely coupled FSI with full fluid domain can give the most solutions and therefore, its results can be taken as standard for comparison with other two methods. With this assumption, it can be observed that profile curves of closely coupled FSI with reduced fluid domain case closely follow the standard curves. However, the curves for loosely coupled FSI are relatively off. Root mean square (rms) values of cross flow amplitudes ($(y/D)_{rms}$), rms values of coefficients of lift ($C_{L_{rms}}$) and mean values of coefficients of drag ($\bar{C}_D$) for different FSI algorithms are compared in Table 5. It can be observed that the results for closely coupled FSI with reduced and full fluid domain are very close to each other. However, the values for loose coupling case

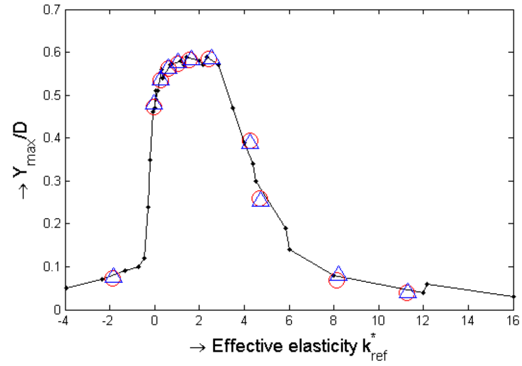

(a) Crossflow amplitudes

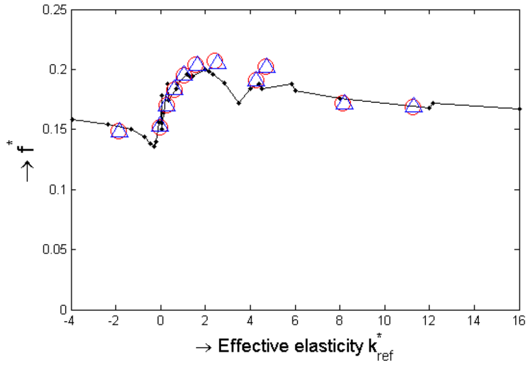

(b) Normalized vortex frequency

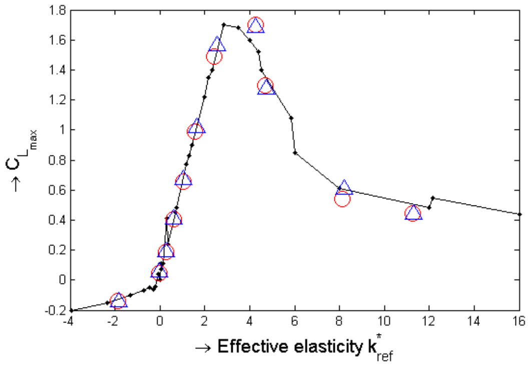

(c) Maximum lift coefficient

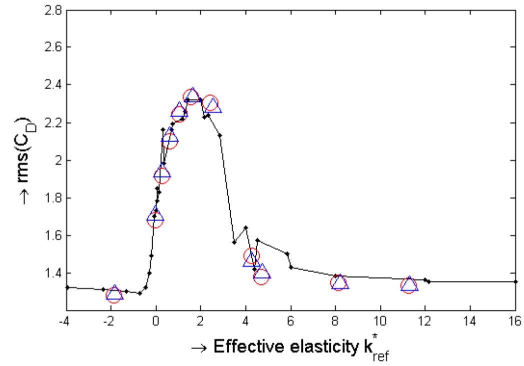

(d) rms of drag coefficient

Fig. 19 1-DoF cylindrical vibration at Re=100: Variation of parameters with effective elasticity (k^*_{eff}) (—●—Shiels et al. [50], O Present work (*Ordered* grid), △ Present work (*Randomized* grid)

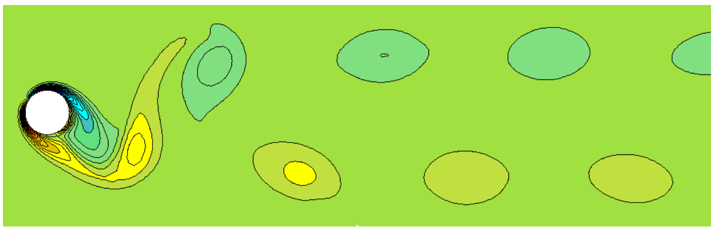

(a) Vorticity at $k^*_{eff} = 1.57$

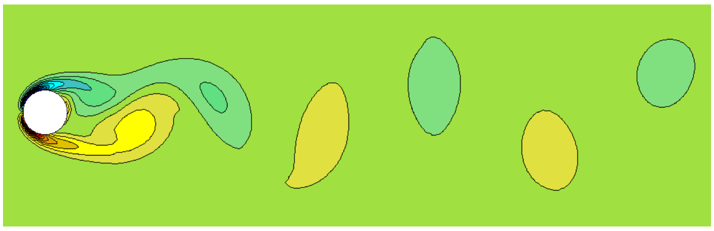

(b) Vorticity at $k^*_{eff} = -1.89$

Fig. 20 Comparison of vorticity plots for 'lock-in' and 'un-locked' configurations

are relatively off. Table 5 also shows computation time per time-step iteration on Intel®Core-i5, 3.1 GHz processor for each case. It can be observed that the computational time is for reduced fluid domain case is only 26% higher than that for loosely coupled case but significantly less than full fluid domain

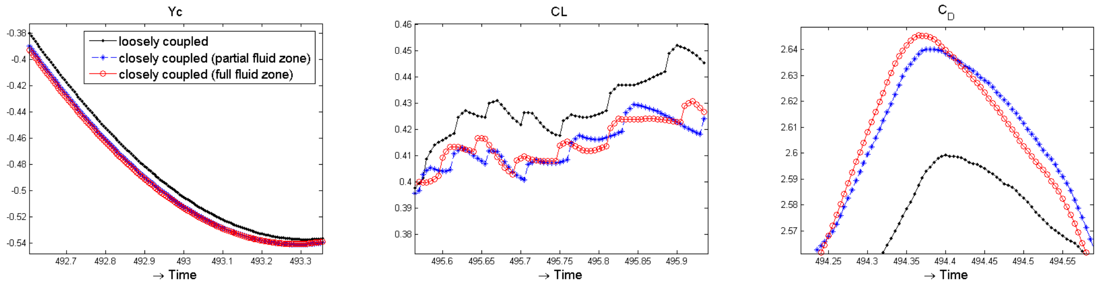

(a) y_c (b) C_L (c) C_D

Fig. 21 1-DoF cylindrical vibration at Re=100: Comparison of time profiles of displacement, lift and drag for i) loosely coupled (—•—), ii) closely coupled with reduced fluid domain (—*—) and iii) closely coupled with full fluid domain (—o—) FSI cases. $k^*_{eff} = 0.623$

Table 5 Comparison of rms values of cross flow amplitudes ($(y/D)_{rms}$), rms values of coefficients of lift ($C_{L_{rms}}$), mean values of coefficients of drag ($\bar{C}_D$) and computational time for different FSI algorithms (cylindrical vibration case with 1-DoF)

Parameter	Loosely coupled FSI	Closely coupled FSI (Reduced fluid domain)	Closely coupled FSI (Full fluid domain)
$(y/D)_{rms}$	0.3802	0.3841	0.3840
$C_{L_{rms}}$	0.3426	0.3338	0.3331
C_D	1.9526	1.9723	1.9718
Compute time (per iteration)	123 m sec	156 m sec	236 m sec

Table 6 Norm-2 of error of cross flow amplitudes ($\|(y/D) - (y/D)_{ref}\|_2$), coefficients of lift ($\|C_L - CL_{ref}\|_2$) and coefficients of drag ($\|C_D - CD_{ref}\|_2$) for different FSI algorithms (cylindrical vibration case with 1-DoF). Results for closely coupled FSI with full fluid domain are used as reference values for calculating the error

Parameter	Loosely coupled FSI	Closely coupled FSI (Reduced fluid domain)
$\|(y/D) - (y/D)_{ref}\|_2$	0.0121	0.0033
$\|C_L - CL_{ref}\|_2$	0.0156	0.0060
$\|C_D - CD_{ref}\|_2$	0.0381	0.0125

case. Table 6 shows Norm-2 of error of cross flow amplitudes ($\|(y/D) - (y/D)_{ref}\|_2$), coefficients of lift ($\|C_L - CL_{ref}\|_2$) and coefficients of drag ($\|C_D - CD_{ref}\|_2$) for loosely coupled FSI and closely coupled FSI with reduced fluid domain. For the purpose of calculating errors, results from closely coupled FSI with full fluid domain are used as reference values. Results show significantly lower errors for closely coupled case with reduced fluid domain. Comparing error values and computation time, it can be seen that closely coupled FSI case with reduced fluid domain calculations offer an efficient computation of FSI problems without much loss in accuracy.

4.2.3 Vortex induced vibration of cylinder with 2-DoF

Vortex induced vibration (VIV) of cylinder with two degrees of freedom is of practical importance in many engineering applications including offshore cylindrical structures, underwater flexibly mounted pipelines and large electrical cables. For flexibly mounted cylindrical objects, incoming flow can initiate modes of vibration both along the flow as well as in cross-flow directions. The problem is therefore often studied at 2-DoF VIV [11,10] and system vibrational response is studied with changing reduced velocity ($v_r = U/(f_N D)$, where U is free stream velocity, D is cylindrical diameter and f_N is natural frequency of vibration). The in-flow vibration of cylinder has been found to show significantly higher amplitudes when ratio of in-line to transverse natural frequencies (f_{Nx}/f_{Ny}) is set around 2.0 due to dual resonant response [10]. For other frequency ratios, cylindrical vibration is predominantly cross-flow and very low amplitudes of in-flow vibrations are observed.

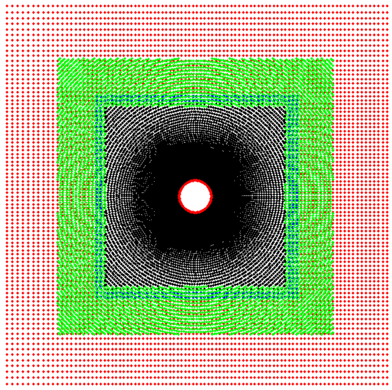

Fig. 22 Grid around cylinder vibrating with 2 degrees of freedom

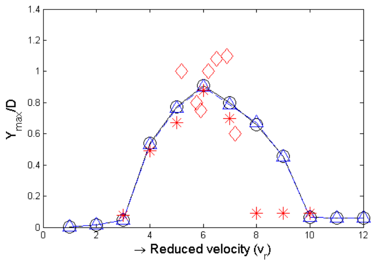

(a) Crossflow amplitudes

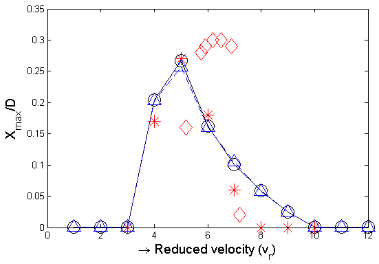

(b) Inflow amplitudes

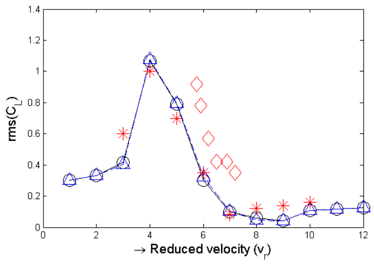

(c) Lift coefficient

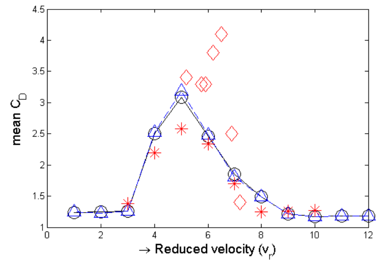

(d) Drag coefficient

Fig. 23 Variation of parameters with reduced velocity (v_r) for cylindrical vibration with 2-DoF (Mass ratio= $m^* = 2.0$, frequency ratio= $f_{Nx}/f_{Ny} = 2.0$, $Re = 150$), —o —present results (*ordered* meshfree nodes), —△ —present results (*randomized* meshfree nodes), $*$ results from [11] (at $= m^* = 2.0$, $= f_{Nx}/f_{Ny} = 2.0$, $Re = 150$), $\diamond$ Experimental results from [10] (at $= m^* = 5.7$, $= f_{Nx}/f_{Ny} = 1.9$, $Re = 15000 - 60000$)

The numerical simulations are carried out for flow, at Reynolds number 150, around a cylinder which has degree of freedom along X (in-flow) as well as Y (cross-flow) direction. Size of active meshfree zone around the cylinder is set as $3D \times 3D$ for this case. Beyond active zone, an overlapped meshfree zone extends by a length of $1.5D$, along all four directions, to cater for solid motion as shown in Fig. 22. Numerical tests are carried out to study the effects of changing reduced velocity (v_r), frequency ratio (f_{Nx}/f_{Ny}) and mass ratio (m^* is the ratio mass of cylinder to the displaced fluid mass). Validation test case is run for mass ratio $m^* = 2.0$ and frequency ratio $f_{Nx}/f_{Ny} = 2.0$. Reduced velocity (v_r) is calculated according to transverse natural frequency (f_{Ny}) and tests are conducted for $v_r = 1 - 12$. Damping is set as zero. Solutions are obtained for both *ordered* and *randomized* meshfree nodal arrangements. Resultant amplitudes of cross-flow and in-flow vibration, root mean square (rms) values of lift coefficient and mean values drag coefficient are shown in Fig. 23 along with numerical

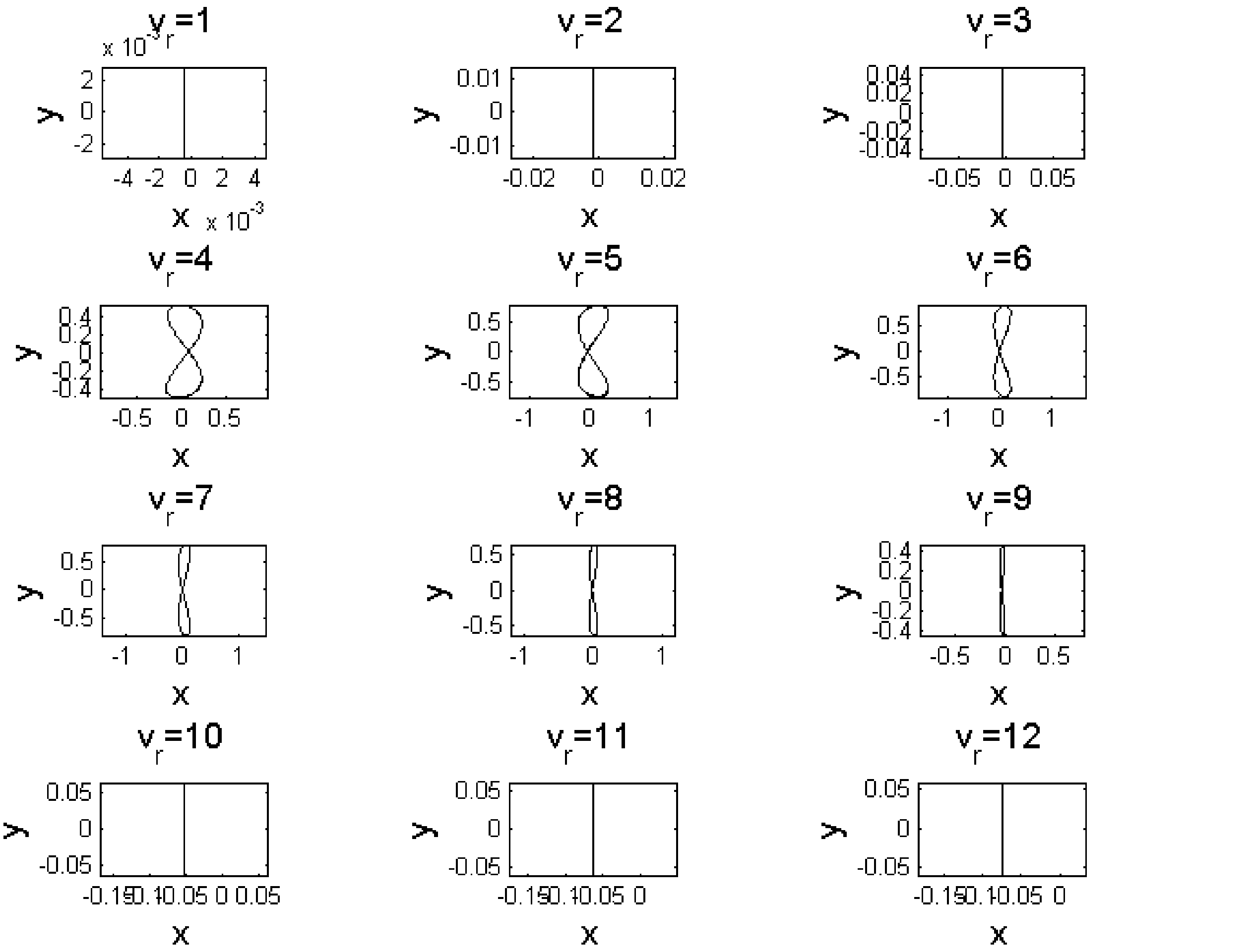

Fig. 24 Cylindrical trajectories for 2-DoF problems. (Mass ratio= $m^* = 5.0$, frequency ratio= $f_{Nx}/f_{Ny} = 2.0$, $Re = 150$)

solutions obtained by Dai [11] and experimental results from Dahl et al. [10]. It can be observed that the results do not change significantly with randomization of meshfree nodes. Vibration amplitudes and lift and drag coefficients tend to increase dramatically as the resonance conditions are approached near $vr = 6$. However, in-flow vibration amplitudes are almost zero away from $vr = 6$. Even cross-flow amplitudes are also very low outside the resonance range. These observations are in agreement with the results of Dahl et al. [10] and Dai [11]. XY trajectories of cylinder at different reduced velocities are plotted in Fig. 24. Maximum in-flow amplitude occurs at $v_r = 5.0$. The value of X_{max}/D is 0.267. Cross-flow amplitudes achieve their maximum value ($Y_{max}/D = 0.908$) at $v_r = 6.0$. These results are similar to those in [10] and [11]. Maximum (rms and mean) values of lift and drag coefficients are also consistent with the solutions of Dai [11].

The effect of changing frequency ratio on system response (amplitudes of aerodynamic forces and solid motion) along in-flow and cross-flow directions is investigated by running the test cases at $f_{Nx}/f_{Ny} = 1.0,\ 1.5$ and 2.0. Mass ratio is set as 1.25. Fig. 25 shows response curves at various reduced velocities v_r and frequency ratios. High vibrational amplitudes (both cross-flow and in-flow directions) are observed for range of reduced velocities $4 \leq v_r \leq 9$ indicating the presence of resonance zone in both directions. Although this resonance zone is present at all tested values of frequency ratio, the vibration amplitudes dramatically increase typically at $= f_{Nx}/f_{Ny} = 2.0$. This increase is more pronounced for in-flow amplitudes where maximum vibrational amplitude soared by 3.4 times when frequency ratio was increased from 1.5 to 2.0. An increase of 1.25 times was observed in maximum

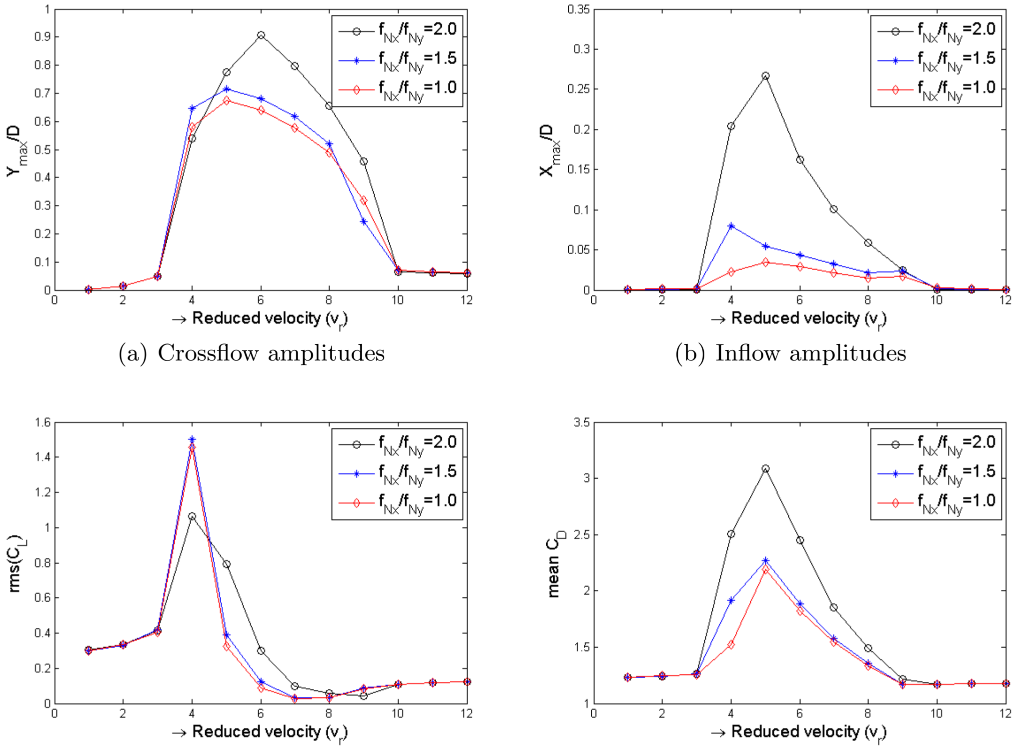

(a) Crossflow amplitudes

(b) Inflow amplitudes

(c) RMS of Lift coefficient

(d) Mean Drag coefficient

Fig. 25 Variation in system response with changing frequency ratio (f_{Nx}/f_{Ny}) for cylindrical vibration with 2-DoF at $= m^* = 1.25$ and $Re = 150$. $-o-$ $f_{Nx}/f_{Ny} = 2.0$, $-*-$ $f_{Nx}/f_{Ny} = 1.5$, $-\diamond-$ $f_{Nx}/f_{Ny} = 1.0$

cross-flow amplitude for same variation of frequency ratio. Moreover, reduced velocity corresponding to maximum vibrational amplitude tends to shift to higher value with increasing frequency ratio. However, bounds of resonant zone remain unaffected during this change.

Fig. 25(c) indicate that lift coefficient largely remains unaffected by variation of frequency ratio except at $= f_{Nx}/f_{Ny} = 2.0$. At this value, significant reduction in the maximum value of C_L is observed. On the contrary, coefficient of drag coefficient depicts an increase in its maximum value at same frequency ratio.

The effect of changing mass ratio on system response has been investigated at $f_{Nx}/f_{Ny} = 2.0$. At these settings, the solution parameters are obtained for different values of mass ratio and for changing reduced velocities. The results are summarized in the plots shown in Fig. 26. The most prominent effect of changing mass ratio is that the resonance zone tends to shrink with increasing mass ratios. Though the peak values appear at same location (i.e same value of v_r), the lower and upper limits of high amplitude regime tend to squeeze inward with increasing mass ratio. The maximum vibration amplitudes remains largely unchanged until $m^* = 2.0$. However, they start to decline later and relatively lower amplitudes (both in-flow and cross-flow) are observed at $m^* = 7.5$. Mass ratio seems to have significant effect on lift coefficient. The maximum value of lift coefficient keeps increasing from $m^* = 0.75$ to $m^* = 2.0$. However, dramatic decline in lift coefficient is observed at $m^* = 7.5$. Moreover, the value of reduced velocity, corresponding to highest value of C_L, also shifts from 4.0 to 5.0. Beyond the resonance zone ($v_r \geq 10$), RMS value of C_L depicts a steadily increasing trend with increasing mass ratio whereas cross-flow amplitudes decrease during same range of v_r.

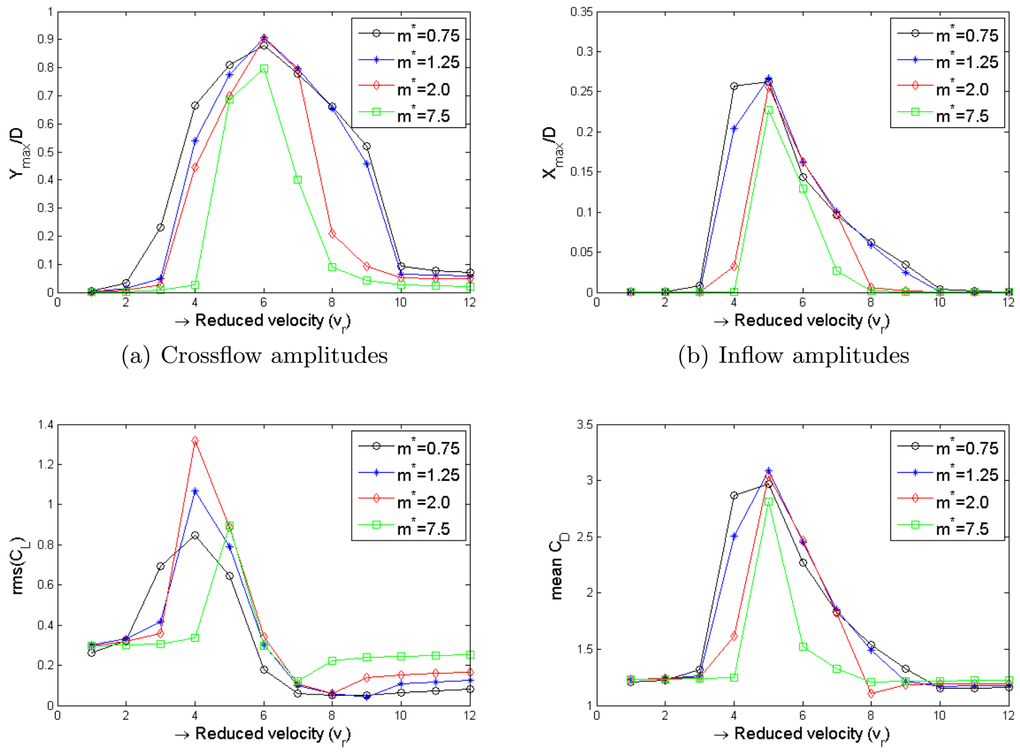

(a) Crossflow amplitudes

(b) Inflow amplitudes

(c) RMS of Lift coefficient

(d) Mean Drag coefficient

Fig. 26 Variation in system response with changing mass ratio for cylindrical vibration with 2-DoF at $f_{Nx}/f_{Ny} = 2.0$ and $Re = 150$. $-o-$ $m^* = 0.75$, $-*-$ $m^* = 1.25$, $-\diamond-$ $m^* = 2.0$, $-\square-$ $m^* = 7.5$

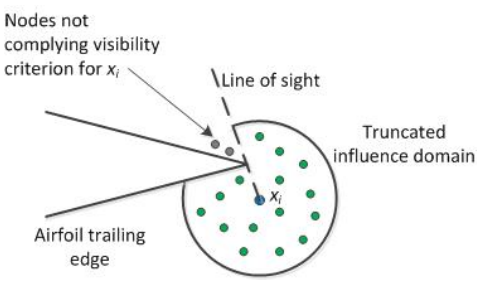

Fig. 27 Influence domain truncated as per visibility criterion near trailing edge of airfoil

4.3 Flow around airfoil

4.3.1 Flow around airfoil in pitch and heave motion

The coupled meshfree-mesh based solver is now used for flow around NACA0015 airfoil which is undergoing simultaneous pitching and heaving motion. Pitch and heave motions of the airfoil are defined by the following equations:

$$\theta(t) = \theta_0 \sin(\omega t) \tag{30}$$
$$h(t) = H_0 \sin(\omega t + \Phi) \tag{31}$$

where θ_0 and H_0 are maximum pitch and heave amplitudes and Φ is the phase difference between pitch and heave motion. Heave amplitude is fixed at $H_0/c = 1.0$ and phase difference $\Phi = -\pi/2$ is used.

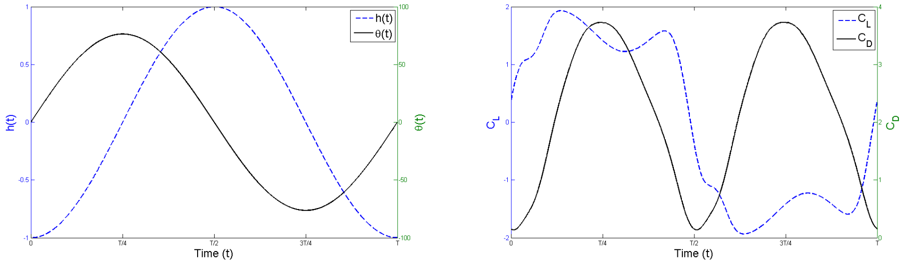

(a) Pitch and heave displacement

(b) Aerodynamic forces

Fig. 28 Variation of displacement and aerodynamic force coefficients around NACA0015 at $Re = 1100,\ \theta_0 = 76.33^o,\ \omega = 0.28\pi$

The tests are conducted at $Re = 1100$ ($Re = \rho U c/\mu$ where, c is the airfoil chord length and U is the free stream velocity). The flow is predominantly laminar at this Reynolds number. Similar tests were conducted by Kinsey and Dumas [36].

Grid configuration is the same as in Fig. 5 while closer view of meshfree nodal arrangement near the airfoil surface is shown in Fig. 8. The Airfoil is placed at a distance of $4c$ from inlet and $12c$ from outlet. Width of fluid domain is set as $10c$. Dimensions of active meshfree zone around airfoil are set as $1.35c \times 1.6c$. The boundary conditions are applied as mentioned in Section 2.1. At airfoil surface, the flow velocity, at next time step ($\mathbf{u}^{n+1}$), is set equal to the velocity of moving boundary node. Intermediate velocity field is then calculated using Eq. (8). Finally, the pressure values at the boundary is obtained using Eq. (9). In order to apply Neumann boundary condition for pressure, at airfoil surface, orthogonal arrangement of nodes is used for the first two layers of meshfree nodes next to the airfoil surface.

An important aspect to be considered here is the treatment of influence domain for meshfree nodes near trailing edge of the airfoil which acts as a non-convex boundary. The influence domains for such nodes are modified according to visibility method suggested by Belytschko et al. [1]. For this purpose, the influence domain of any meshfree node $\mathbf{x}_i$ is truncated in such a manner that only those neighbouring nodes fall in the influence domain which can be linked with $\mathbf{x}_i$ through a straight line without intersecting the boundary. The truncated influence domain near convex boundary is shown in Fig. 27.

The problem is set up in a way that heave reference frame is attached with the airfoil. In this manner, the airfoil performs pitching motion in a heaving reference frame. The heaving displacement is therefore, not imparted to the moving mesh. The movement of mesh is accomplished by displacing the grid nodes (of meshfree zone) only according to prescribed pitching motion. However, heave velocity does contribute in the vertical component of ALE velocity when formulating momentum equation (Eq. (5)) in ALE formulation. Similar strategy was used by Kinsey and Dumas [36] in their work. Numerical simulations are carried out at $\theta_0 = 76.33^o$ and $\omega = 0.28\pi$. Time step is set as $\Delta t = 10^{-3}$ sec.

Variation of heave and pitch displacements in a single oscillation period of airfoil, for $\theta_0 = 76.33^o$, $\omega = 0.28\pi$ case, is shown in Fig. 28(a). Variation of aerodynamic forces (C_L and C_D) during same period is plotted in Fig. 28(b). Vorticity profiles around the airfoil at different stages of periodic motion are shown in Fig. 29. As the pitch angle is increased in the initial phase of oscillation, the lift achieves its maximum value. The flow remains largely attached with airfoil top surface for $t < T/8$ as shown in Fig. 29(a). The first peak in lift profile appears at around $t = T/8$. Increasing lift also causes increase in pressure drag and therefore, drag coefficient also increases. This initial rise in lift is followed by flow separation close to leading edge as shown in Fig. 29(b) and causes reduction in lift. Subsequently, the detached leading edge vortex re-attaches with the airfoil close to its trailing edge (Fig. 29(c)) at about $t = 3T/8$ causing a second peak in the lift profile. However, as the leading edge vortex leaves the airfoil from trailing edge and moves further downstream, a sharp decline in lift is observed between $T3T/8 < t < 5T/*$. The lift coefficient reduce to zero and then shows similar profile in negative direction. These results are in good agreement with the reference values from [36].

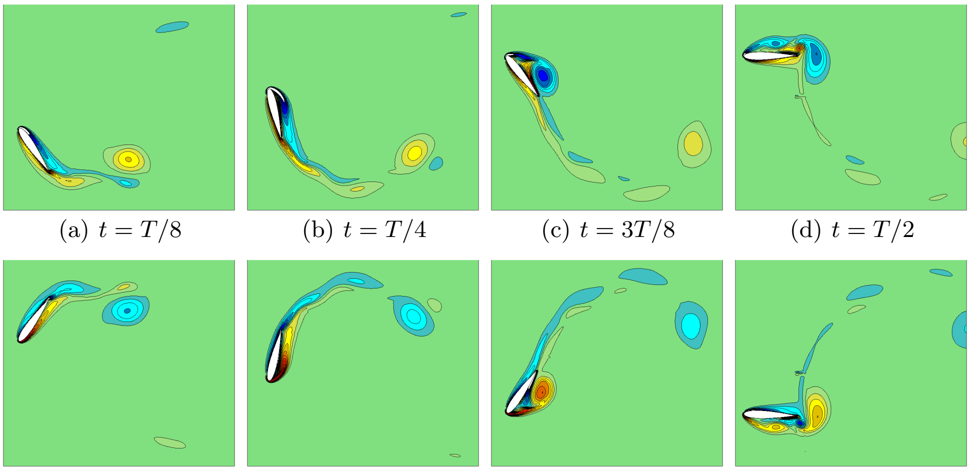

(a) $t = T/8$ (b) $t = T/4$ (c) $t = 3T/8$ (d) $t = T/2$

(e) $t = 5T/8$ (f) $t = 3T/4$ (g) $t = 7T/8$ (h) $t = T$

Fig. 29 Instantaneous vorticity profiles around NACA0015 at $Re = 1100$, $\theta_0 = 76.33^o$, $\omega = 0.28\pi$

Table 7 Comparison of maximum values of coefficients of lift ($C_{L_{max}}$), mean values of coefficients of drag ($\bar{C}_D$) and maximum values of coefficients of lift ($C_{M_{max}}$) for pitching-motion-activated-flapping NACA0015 airfoil

Mechanical Parameters	Source	Re	$C_{L_{max}}$	C_D	$C_{M_{max}}$
$\theta_0 = 15^o$, $f^* = 0.2$, $d^* = 2\pi$, $k^* = 10$, $m^* = 1$	Wu et al. [61]	1100	0.704	0.179	-
	Present work	1100	0.69	0.17	-
$\theta_0 = 30^o$, $f^* = 0.1$, $d^* = \pi$, $k^* = 0$, $m^* = 1$	Wu et al. [61]	1100	0.905	0.345	-
	Present work	1100	0.885	0.334	-
$\theta_0 = 75^o$, $f^* = 0.12$, $d^* = \pi$, $k^* = 0$, $m^* = 0.1022$	Deng et al. [15]	1000	2.0	-	0.33
	Present work	1000	2.017	-	0.31
$\theta_0 = 75^o$, $f^* = 0.22$, $d^* = \pi$, $k^* = 0$, $m^* = 0.1022$	Deng et al. [15]	1000	2.8	-	0.6
	Present work	1000	2.55	-	0.56

4.3.2 Pitching-motion-activated-flapping airfoil

Semi-activated flapping airfoil system is studied here. In this case, the airfoil is subjected to a prescribed pitching motion about its elastic axis and is allowed move freely along heave axis due to fluid forces. Airfoil is mounted on a translational spring-damper system. When, airfoil is subjected to periodic pitch oscillation, it causes corresponding variation of fluid forces over time. These time varying fluid forces induce heaving motion. Such mechanisms have recently gained focus for their potential application in tidal and wind energy extraction systems [61,15]. Pitch displacement ($\theta(t)$) for the airfoil is defined by Eq. (30). Resulting heave displacement is calculated using Eq. (19). Solid equations are solved in non-dimensionalized form. The non-dimensionalized mass (m^*), damping (d^*) and spring stiffness (k^*) are defined as:

$$m^* = \frac{m}{\frac{1}{2}\rho c^2},\ d^* = \frac{d}{\frac{1}{2}\rho U c},\ k^* = \frac{k}{\frac{1}{2}\rho U^2}$$

where ρ, U and c are flow density, free stream velocity and airfoil chord length respectively. The test cases are run for flow around NACA0015 airfoil. with its elastic axis located at a distance $c/3$ from leading edge. Results are obtained at $Re = 1100$ and $Re = 1000$. Laminar flow equations can safely be used at this Reynolds number. Simulations are run at four different sets of mechanical parameters (θ_0, f^*, d^* k^*, m^*) and resultant values are summarized in Table 7. The results are compared with the solutions from Wu et al. [61] and Deng et al. [15] respectively and are found to be in good agreement with the previous studies. Variation of C_L during a single pitch oscillation period is compared, in Fig. 30, for both test cases conducted at $Re = 1000$. It can be observed that the peak value of lift coefficient increases at higher frequency (f^*). Similar behaviour was observed by Wu et al. [61] in their work.

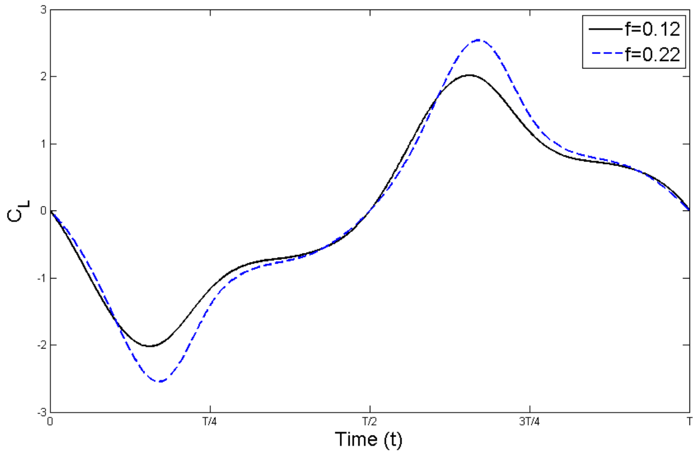

Fig. 30 Variation of coefficient of lift C_L around pitching-motion-activated flapping NACA0015 airfoil during a single oscillation period ($Re = 1000,\ \theta_0 = 75^o,\ k^* = 0,\ d^* = \pi, m^* = 0.1022$)

Above calculations are carried out using closely coupled FSI with partial fluid domain. Calculation for simulation time of 0.1 sec were performed in 295 sec on Intel®2.4 GHz processor. On the contrary, similar calculations for full fluid domain were carried out in 840 sec on same machine. Therefore, the computation time was reduced by 65 percent by reducing the fluid domain for inner FSI iterations.

5 Conclusion

This paper presents a coupled meshfree-mesh based solution scheme on hybrid grid for dealing with flow around moving solid objects. Fluid-solid interaction has been implemented using partitioned approach. Flow equations, in ALE formulation are solved by local RBF-FD on moving meshfree nodes, and conventional finite differencing on static Cartesian grid is used for flow equations in Eulerian formulation. The equations for solid motion are solved using Runge-Kutta method.

In current work, a modular approach has been employed for solution of momentum as well as pressure Poisson equations in different fluid zones. The governing equations, for both velocity and pressure, are iteratively solved in meshfree and Cartesian zones. In this regard, another approach is to set up a single pressure problem in the entire fluid domain. The pressure Poisson equation can then be solved, for both (meshfree and Cartesian) zones, simultaneously. An improved accuracy may be achieved by using this approach. However, simultaneous solution for pressure will compromise the modular characteristics of the solution scheme. Currently, the meshfree and mesh based solvers run independent to each other exchanging data at the interface nodes. Simultaneous solution of pressure equations over the entire domain would require the derivation of a separate pressure equation applicable to all the zones. Further work can however be conducted to further explore this aspect.

Various techniques have been employed during current solution scheme to improve the performance and accuracy. Adaptive sizing of influence domain, for meshfree nodes, has allowed to vary nodal density without affecting the well conditioning of RBF coefficient matrices. Use of partial fluid domain made it possible to improve the cohesiveness of fluid and structural solver at interface boundary with relatively smaller computational cost. The scheme was successfully applied to problems with rigid solids with one and two degrees of freedom. Coupling of meshfree and mesh based solver over hybrid fluid grid has been found to be an efficient way of optimizing the inherent strengths of both methods. Future work in this regard may focus on the use of stabilization techniques for high Reynolds number flows, turbulent modelling and flexible structures.

References

References

1. Belytschko, T., Lu, Y.Y., Gu, L.: Element-free Galerkin methods. International Journal for Numerical Methods in Engineering **37**(2), 229–256 (1994). DOI 10.1002/nme.1620370205. URL http://dx.doi.org/10.1002/nme.1620370205
2. Braza, M., Chassaing, P., Minh, H.H.: Numerical study and physical analysis of the pressure and velocity fields in the near wake of a circular cylinder. Journal of fluid mechanics **165**, 79–130 (1986)
3. C. Shu, H.D., Yeo, K.S.: Local radial basis function-based differential quadrature method and its application to solve two-dimensional incompressible navier-stokes equations. Computer Methods in Applied Mechanics and Engineering **192**(7-8), 941–954 (2003)
4. Chen, W., Tanaka, M.: A meshless, integration-free, and boundary-only RBF technique. Computers and Mathematics with Applications **43**(3-5), 379–391 (2002)
5. Chesshire, G., Henshaw, W.D.: Composite overlapping meshes for the solution of partial differential equations. Journal of Computational Physics **90**(1), 1–64 (1990)
6. Chew, C.S., Yeo, K.S., Shu, C.: A generalized finite-difference (GFD) ALE scheme for incompressible flows around moving solid bodies on hybrid meshfreecartesian grids. Journal of Computational Physics **218**(2), 510–548 (2006)
7. Chorin, A.J.: Numerical study of slightly viscous flow. Journal of Fluid Mechanics **57**, 785–796 (1973)
8. Chow, P., Addison, C.: Putting domain decomposition at the heart of a mesh-based simulation process. International journal for numerical methods in fluids **40**(12), 1471–1484 (2002)
9. Clarke, D.K., Hassan, H., Salas, M.: Euler calculations for multielement airfoils using cartesian grids. AIAA journal **24**(3), 353–358 (1986)
10. Dahl, J., Hover, F., Triantafyllou, M., Oakley, O.: Dual resonance in vortex-induced vibrations at subcritical and supercritical reynolds numbers. Journal of Fluid Mechanics **643**, 395–424 (2010)
11. Dai ZHOU Jiahuang TU, Y.B.: Two degrees of freedom flow-induced vibrations on a cylinder. In: 7th International colloquium on bluff body aerodynamics and applications BBAA7, International association for wind engineering. American Institute of Aeronautics and Astronautics (2012)
12. De Rosis, A., Falcucci, G., Ubertini, S., Ubertini, F.: A coupled lattice Boltzmann-finite element approach for two-dimensional fluid-structure interaction. Computers and Fluids **86**(0), 558–568 (2013)
13. De Zeeuw, D., Powell, K.G.: An adaptively refined cartesian mesh solver for the euler equations. AIAA Paper (91-1542) (1991)
14. Degroote, J., Bruggeman, P., Haelterman, R., Vierendeels, J.: Stability of a coupling technique for partitioned solvers in {FSI} applications. Computers and Structures **86**(2324), 2224 – 2234 (2008). DOI http://dx.doi.org/10.1016/j.compstruc.2008.05.005. URL http://www.sciencedirect.com/science/article/pii/S0045794908001466
15. Deng, J., Teng, L., Pan, D., Shao, X.: Inertial effects of the semi-passive flapping foil on its energy extraction efficiency. Physics of Fluids (1994-present) **27**(5), 053,103 (2015)
16. Dennis, S., Chang, G.Z.: Numerical solutions for steady flow past a circular cylinder at Reynolds numbers up to 100. J. Fluid Mech **42**(3), 471–489 (1970)
17. Ding, H., Shu, C., Yeo, K.S., Xu, D.: Simulation of incompressible viscous flows past a circular cylinder by hybrid FD scheme and meshless least square-based finite difference method. Computer Methods in Applied Mechanics and Engineering **193**(9-11), 727–744 (2004)
18. Dowell, E., Hall, K.: Modeling of fluid-structure interaction. Annual Review of Fluid Mechanics **33**(1), 445–490 (2001)
19. Farhat, C., Lesoinne, M., Le Tallec, P.: Load and motion transfer algorithms for fluid/structure interaction problems with non-matching discrete interfaces: Momentum and energy conservation, optimal discretization and application to aeroelasticity. Computer Methods in Applied Mechanics and Engineering **157**(12), 95–114 (1998)
20. Farhat, C., Lesoinne, M., Maman, N.: Mixed explicit/implicit time integration of coupled aeroelastic problems: Threefield formulation, geometric conservation and distributed solution. International Journal for Numerical Methods in Fluids **21**(10), 807–835 (1995)
21. Farhat, C., van der Zee, K.G., Geuzaine, P.: Provably second-order time-accurate loosely-coupled solution algorithms for transient nonlinear computational aeroelasticity. Computer Methods in Applied Mechanics and Engineering **195**(1718), 1973–2001 (2006)
22. Feistauer, M., Horacek, J., Ruzicka, M., Sváček, P.: Numerical analysis of flow-induced nonlinear vibrations of an airfoil with three degrees of freedom. Computers and Fluids **49**(1), 110–127 (2011)
23. Firoozjaee, A.R., Afshar, M.H.: Steady-state solution of incompressible Navier-Stokes equations using discrete least-squares meshless method. International Journal for Numerical Methods in Fluids **67**(3), 369–382 (2011)
24. Fornberg, B.: A numerical study of steady viscous flow past a circular cylinder. Journal of Fluid Mechanics **98**(04), 819–855 (1980)
25. Franke, C., Schaback, R.: Solving partial differential equations by collocation using radial basis functions. Applied Mathematics and Computation **93**(1), 73–82 (1998)
26. Glowinski, R., Pan, T.W., Periaux, J.: A fictitious domain method for external incompressible viscous flow modeled by navier-stokes equations. Computer Methods in Applied Mechanics and Engineering **112**(1), 133–148 (1994)

27. Hinatsu, M., Ferziger, J.: Numerical computation of unsteady incompressible flow in complex geometry using a composite multigrid technique. International Journal for Numerical Methods in Fluids **13**(8), 971–997 (1991)
28. Hirt, C., Amsden, A., Cook, J.: An arbitrary Lagrangian-Eulerian computing method for all flow speeds. Journal of Computational Physics **14**(3), 227–253 (1974). DOI http://dx.doi.org/10.1016/0021-9991(74)90051-5. URL http://www.sciencedirect.com/science/article/pii/0021999174900515
29. Ii, S., Sugiyama, K., Takeuchi, S., Takagi, S., Matsumoto, Y.: An implicit full Eulerian method for the fluid-structure interaction problem. International Journal for Numerical Methods in Fluids **65**(1-3), 150–165 (2011)
30. Javed, A., Djidjeli, K., Xing, J.T., Sun, Z.: An ALE Based Hybrid Meshfree Local RBF-Cartesian FD scheme for Incompressible flow around moving boundaries. AIAA Aviation. American Institute of Aeronautics and Astronautics (2014). Doi:10.2514/6.2014-2312
31. Javed, A., Djijdeli, K., Xing, J.T.: Shape adaptive RBF-FD implicit scheme for incompressible viscous Navier-Stokes equations. Computers and Fluids **89**(0), 38–52 (2014)
32. Kamakoti, R., Shyy, W.: Fluid-structure interaction for aeroelastic applications. Progress in Aerospace Sciences **40**(8), 535–558 (2004)
33. Kansa, E.J.: Multiquadrics - a scattered data approximation scheme with applications to computational fluid-dynamics .2. solutions to parabolic, hyperbolic and elliptic partial-differential equations. Computers and Mathematics with Applications **19**(8-9), 147–161 (1990)
34. Kim, D., Choi, H.: A second-order time-accurate finite volume method for unsteady incompressible flow on hybrid unstructured grids. Journal of Computational Physics **162**(2), 411–428 (2000)
35. Kim, J., Moin, P.: Application of a Fractional-Step method to incompressible Navier-Stokes equations. Journal of Computational Physics **59**(2), 308–323 (1985)
36. Kinsey, T., Dumas, G.: Parametric study of an oscillating airfoil in a power-extraction regime. AIAA journal **46**(6), 1318–1330 (2008)
37. Liu, C., Zheng, X., Sung, C.: Preconditioned multigrid methods for unsteady incompressible flows. Journal of Computational Physics **139**(1), 35–57 (1998)
38. Mai-Duy, N., Tran-Cong, T.: Numerical solution of differential equations using multiquadric radial basis function networks. Neural Networks **14**(2), 185–199 (2001)
39. Mittal, S., Kumar, V.: Flow-induced vibrations of a light circular cylinder at Reynolds numbers 10^3 to 10^4. Journal of Sound and Vibration **245**(5), 923–946 (2001)
40. P. Phani Chinchapatnam, K.D., Nair, P.B.: Radial basis function meshless method for the steady incompressible NavierStokes equations. International Journal of Computer Mathematics **84**(10), 1509–1521 (2007)
41. P. Phani Chinchapatnam K. Djidjeli, P.B.N., Tan, M.: A compact RBF-FD based meshless method for the incompressible Navier-Stokes equations. pp. 275–290 (2009)
42. Park, K.: Partitioned transient analysis procedures for coupled-field problems: stability analysis. Journal of Applied Mechanics **47**(2), 370–376 (1980)
43. Perng, C., Street, R.: A coupled multigrid-domain-splitting technique for simulating incompressible flows in geometrically complex domains. International journal for numerical methods in fluids **13**(3), 269–286 (1991)
44. Picano, F., Breugem, W.P., Brandt, L.: Turbulent channel flow of dense suspensions of neutrally buoyant spheres. Journal of Fluid Mechanics **764**, 463–487 (2015)
45. Piperno, S., Farhat, C., Larrouturou, B.: Partitioned procedures for the transient solution of coupled aroelastic problems part i: Model problem, theory and two-dimensional application. Computer Methods in Applied Mechanics and Engineering **124**(12), 79–112 (1995)
46. Placzek, A., Sigrist, J.F., Hamdouni, A.: Numerical simulation of an oscillating cylinder in a cross-flow at low Reynolds number: Forced and free oscillations. Computers & Fluids **38**(1), 80–100 (2009)
47. Saad, Y., Schultz, M.H.: Gmres: A generalized minimal residual algorithm for solving nonsymmetric linear systems. SIAM Journal on scientific and statistical computing **7**(3), 856–869 (1986)
48. Sanyasiraju, Y., Chandhini, G.: Local radial basis function based gridfree scheme for unsteady incompressible viscous flows. Journal of Computational Physics **227**(20), 8922–8948 (2008)
49. Schaback, R.: Error estimates and condition numbers for radial basis function interpolation. Advances in Computational Mathematics **3**(3), 251–264 (1995). DOI 10.1007/BF02432002. URL http://dx.doi.org/10.1007/BF02432002
50. Shiels, D., Leonard, A., Roshko, A.: Flow-induced vibration of a circular cylinder at limiting structural parameters. Journal of Fluids and Structures **15**(1), 3–21 (2001)
51. Sváček, P., Feistauer, M., Horacek, J.: Numerical simulation of flow induced airfoil vibrations with large amplitudes. Journal of Fluids and Structures **23**(3), 391–411 (2007)
52. Takami, H., Keller, H.B.: Steady two-dimensional viscous flow of an incompressible fluid past a circular cylinder. Physics of Fluids **12**(12), II–51–II–56 (1969)
53. Takashi, N., Hughes, T.J.R.: An arbitrary Lagrangian-Eulerian finite element method for interaction of fluid and a rigid body. Computer Methods in Applied Mechanics and Engineering **95**(1), 115–138 (1992)
54. Tang, H., Jones, S.C., Sotiropoulos, F.: An overset-grid method for 3d unsteady incompressible flows. Journal of Computational Physics **191**(2), 567–600 (2003)
55. Tolstykh, A.I., Shirobokov, D.A.: On using radial basis functions in a "finite difference mode" with applications to elasticity problems. Computational Mechanics **33**(1), 68–79 (2003)
56. Tuann, S.y., Olson, M.D.: Numerical studies of the flow around a circular cylinder by a finite element method. Computers & Fluids **6**(4), 219–240 (1978)

57. Uhlmann, M.: An immersed boundary method with direct forcing for the simulation of particulate flows. Journal of Computational Physics **209**(2), 448 – 476 (2005). DOI http://dx.doi.org/10.1016/j.jcp.2005.03.017. URL http://www.sciencedirect.com/science/article/pii/S0021999105001385
58. V. Bayona M. Moscoso, M.C., Kindelan, M.: RBF-FD formulas and convergence properties. Journal of Computational Physics **229**(22), 8281–8295 (2010)
59. Wang, J.G., Liu, G.R.: On the optimal shape parameters of radial basis functions used for 2-D meshless methods. Computer Methods in Applied Mechanics and Engineering **191**(23-24), 2611–2630 (2002)
60. Wright, G.B., Fornberg, B.: Scattered node compact finite difference-type formulas generated from radial basis functions. Journal of Computational Physics **212**(1), 99–123 (2006)
61. Wu, J., Qiu, Y., Shu, C., Zhao, N.: Pitching-motion-activated flapping foil near solid walls for power extraction: A numerical investigation. Physics of Fluids (1994-present) **26**(8), 083,601 (2014)